# CD155 and EndoA1 mediate growth and tissue invasion downstream of MAP4K4 in medulloblastoma cells

Charles Capdeville[1], Linda Russo[1], David Penton[2], Jessica Migliavacca[1], Milica Zecevic[1], Alexandre Gries[1], Stephan C.F. Neuhauss[2], Michael A. Grotzer[3], Martin Baumgartner[1*]

1. Pediatric Molecular Neuro-Oncology Lab, Children's Research Center, University Children's Hospital Zürich, Zürich, Switzerland

2. Department of Molecular Life Sciences, University of Zurich, Zürich, Switzerland

3. Department of Oncology, University Children's Hospital Zürich, Zürich, Switzerland

*Correspondence: Pediatric Molecular Neuro-Oncology Lab, Children's Research Center, University Children's Hospital Zürich, Balgrist Campus, Lengghalde 5, CH-8008 Zürich, Switzerland

CH-8008 Zürich, e-mail: Martin.Baumgartner@kispi.uzh.ch; Tel.: +41 44 266 37 30

Running title: Indirect control of invasion by MAP4K4

Keywords: CD155/PVR, Endophilin A1, MAP4K4, Medulloblastoma, Tissue invasion,

Summary blurb: This study describes kinase-controlled alterations in the membrane proteome of activated tumor cells and identifies two novel regulators of pathogenic growth and tissue invasion in medulloblastoma.

**Abstract**

The composition of the plasma membrane (PM)-associated proteome of tumor cells determines cell-cell and cell-matrix interactions and the response to environmental cues. Whether the PM-associated proteome impacts the phenotype of Medulloblastoma (MB) tumor cells and how it adapts in response to growth factor cues is poorly understood. Using a spatial proteomics approach, we observed that hepatocyte growth factor (HGF)-induced activation of the receptor tyrosine kinase c-MET in MB cells changes the abundance of transmembrane and membrane-associated proteins. The depletion of MAP4K4, a pro-migratory effector kinase downstream of c-MET, leads to a specific decrease of the adhesion and immunomodulatory receptor CD155 and of components of the fast-endophilin-mediated endocytosis (FEME) machinery in the PM-associated proteome of HGF-activated MB cells. The decreased surface expression of CD155 or of the FEME effector Endophilin A1 reduces growth and invasiveness of MB tumor cells in the tissue context. These data thus describe a novel function of MAP4K4 in the control of the PM-associated proteome of tumor cells and identified two downstream effector mechanisms controlling proliferation and invasiveness of MB cells.

## Introduction

The plasma membrane (PM)-associated proteome is a dynamic interface of mammalian cells, which orchestrates interactions with the extracellular environment and transmits extracellular cues. This physical barrier regulates the transfer of chemical and mechanical information between extracellular and intracellular spaces. The net outcome of the functions of PM-associated proteins affects the cellular phenotype and the composition and biophysical structure of the extracellular microenvironment. The PM-associated proteome primarily consists of receptors, cell adhesion molecules, enzymes and ion channels[1], and their expression defines the strength and duration of signal transmission and how the cell interacts with its environment. Besides these transmembrane proteins, numerous proteins are associated with the PM either directly through lipid anchors, or indirectly by binding to transmembrane proteins. The diversity of proteins associated with the PM and their differential expression, localization, or regulation in pathological conditions such as cancer not only constitutes the condition-specific biomarker landscape[2], but also defines a druggable repertoire of therapeutic targets to interfere with the oncogenic phenotype.

The PM-associated proteome of a cell is dynamically controlled through membrane turnover via endocytic uptake and exocytic fusion[3,4], which involves the dynamic reorganization of the cortical cytoskeleton. Membrane trafficking and cytoskeleton reorganization are thus key processes that position chemical and mechanical sensors and enable the uptake of nutrients or extrusion of signal transmitters, thereby determining the cellular response to complex environments. Moreover, endocytosis and the sequential intracellular vesicular trafficking control adhesion turnover, signal transduction, consequently influencing the duration of mitogenic or mobile phenotypes. De-regulation of physiological trafficking in tumor cells may thus contribute to cell transformation[5], and especially altered endocytic activity can broadly impact tumor cell growth, invasion and metastasis, and viability [6,7].

Medulloblastoma (MB) is a malignant embryonal neuroepithelial tumor of the cerebellum with a high propensity to disseminate and metastasize within the central nervous system[8]. Several omics studies described the genomic heterogeneity in MB, which is now classified into four subgroups with twelve subtypes in total[9,10]. Despite this molecular understanding of MB, the current standard therapy

67 still consists of surgical resection of the tumor and craniospinal irradiation followed by chemotherapy[11].
68 These anti-cancer therapies can have a devastating impact on the developing brain of the patients and
69 can cause severe long-term side effects such as cognitive or mobility impairments[12]. Thus, novel
70 therapeutic options with phenotype-specific anti-tumor activity are needed to replace or complement
71 current treatments and reduce therapy-associated side effects.

72 The Ser/Thr kinase MAP4K4 is overexpressed in MB and contributes to the pro-invasive
73 phenotype of MB cells downstream of hepatocyte growth factor (HGF)-cellular mesenchymal-epithelial
74 transition factor (c-MET) stimulation[13,14]. c-MET receptor tyrosine kinase (RTK) activation caused
75 increased membrane dynamics, increased endocytic uptake and the activation and turnover of integrin
76 ß1 adhesion receptor[13]. Integrin activation and internalization of integrins are necessary for cell
77 migration and invasion[15,16]. Internalization of activated RTKs and integrins furthermore modulates
78 pathway activation at endosomal compartments[17,18]. Thereby, the condition-specific endocytic activity
79 adds a layer of regulatory impact on tumor cell behavior.

80 Endocytic cellular processes like synaptic vesicle endocytosis, receptor trafficking, apoptosis
81 and mitochondrial network dynamics can be controlled by endophilins, which are members of the BAR
82 (Bin/amphiphysin/Rvs) domain superfamily [19,20]. Dysregulation of these processes is associated with
83 cancer or neurodegenerative diseases[19,21]. Endophilins were initially considered a peripheral
84 component of clathrin-mediated endocytosis[22,23]. A novel clathrin-independent endocytic pathway
85 based on endophilin A subfamily activity, termed fast endophilin mediated endocytosis (FEME) was
86 described recently[21], and several studies also implicated endophilins in cell motility control[24–26]. The
87 endophilin A1 is almost exclusively expressed in brain tissue[27]

88 How the PM proteome of MB cells is regulated in response to RTK activation, and which
89 potential therapeutic targets may be represented in the dynamic PM compartment are unknown.
90 Therefore, we used a spatial proteomics approach[28] and determined the PM-associated proteome of
91 resting and RTK-activated MB cells. We addressed whether the pro-oncogenic activity of MAP4K4
92 could be coupled to RTK-induced, dynamic alterations in the PM proteome. This analysis allowed the
93 identification of PM-associated proteins subjected to c-MET-induced spatial re-distribution and the
94 identification of MAP4K4 as a regulator of this process. We describe MAP4K4-dependent alterations in
95 PM association of solute carriers, ion channels and of the immune modulatory receptors. Furthermore,

96 we address underlying mechanisms and potential functional consequences of this regulation for cancer
97 cell homeostasis and cancer cell motility.

98

99 **Results**

100 **HGF-c-MET signaling promotes PM proteome reorganization in medulloblastoma cells**

101 To determine changes in PM and PM-proximal association of proteins in response to growth
102 factor stimulation, we used a PM-associated proteome analysis approach (Fig. 1A). We used
103 membrane-impermeable Sulfo-NHS-SS-biotin labeling of intact sgControl (sgCTL, sgC) and
104 sgMAP4K4 (MAP4K4 knockout, sgM4, Fig S1A,B) MB tumor cells, followed by streptavidin protein
105 capture and high-resolution mass spectrometry analysis (Fig. 1A). The data generated a rather diverse
106 set of proteins, which is available via ProteomeXchange with the identifier PXD030597. We observed
107 no significant difference in the PM proteome between sgCTL and sgMAP4K4 cells under starved
108 conditions (Fig. S1C). Stimulation with HGF caused an alteration in protein abundance (Fig. S1C,D),
109 suggesting that growth factor stimulation alters the composition of PM-associated proteins.. To
110 specifically enrich for membrane or membrane-associated proteins, we filtered the data either by using
111 the transmembrane prediction algorithm TMHMM[29] or by annotating the proteins according to their
112 known subcellular localization[30]. These stringent sorting criteria identified 952 TM proteins and 336 PM-
113 annotated proteins, respectively (Fig. 1A, Tables 1 & 2). In sgCTL cells, HGF stimulation decreased the
114 abundance of a number of TM (Fig. 1B, S1D, Table 3) or PM-annotated proteins (Fig. 1B, S1D, Table
115 4). This indicated that either internalization of these proteins in response to c-MET activation is
116 increased or recycling decreased. We previously found that internalization of activated c-MET depends
117 on MAP4K4[13]. Therefore, we tested whether MAP4K4 could contribute to reduced PM association in
118 cells, where c-MET is activated by HGF stimulation. By comparing HGF-stimulated sgCTL and
119 sgMAP4K4 cells, we detected changes in the abundance of >1500 proteins (fold change >2, adjusted
120 p-value <0.2, Fig. 1C, S1F). Specifically, HGF stimulation in MAP4K4 depleted cells led to an increased
121 abundance of TM proteins (Fig. 1B,C, Table 3) and PM-annotated proteins (Fig. 1B,C, Table 4),
122 suggesting a regulatory function of MAP4K4 in PM localization of these proteins. A paradigmatic
123 example is c-MET itself, which is internalized in a MAP4K4-dependent manner in DAOY cells[14] and
124 detected at lower levels in the PM proteome in response to HGF stimulation in sgCTL cells (Fig. 1D).

125 MAP4K4 contributes to this process as depletion of MAP4K4 significantly increases c-MET abundance
126 on the PM in HGF-stimulated cells. None of the five additional RTKs detected by mass-spectrometry
127 displayed similar behavior (Fig. 1D). We concluded from this experiment that c-MET activation triggers
128 the turnover of PM-associated proteins and that MAP4K4 is indispensable for the turnover of a number
129 of those proteins in MB cells. Gene ontology analysis of PM-associated proteins revealed MAP4K4
130 dependencies in several pathways controlling endo- and exocytotic activities of cells as well as immune
131 cell recognition or solute exchange (Fig. 1E). It also revealed that HGF stimulation in sgMAP4K4 cells
132 increased PM association of proteins with reported implications in chemotherapy sensitivity/resistance
133 (SLC29A1, SLC4A7, LRRC8)[31,32] (Fig. 1F, Table 3). Conversely, MAP4K4 depletion decreased PM
134 association of proteins involved in tumor immune evasion (CD155, CD276, HLA-G)[33–35], in solute influx
135 regulation (CLIC1, SLCs, ABCCs)[36,37] and cell migration (CD155, CD276)[33,38] (Fig. 1F, tables 1-4). In
136 conclusion, we found that MET activation by HGF triggers reorganization of the PM-associated
137 proteome in MB cells and that MAP4K4 is involved in the selective control of this process.

138

139 **Altered transporter expression in MAP4K4-depleted cells does not significantly affect sensitivity**
140 **to Etoposide and Lomustine**

141 To better understand which protein functions are particularly affected by the altered PM-
142 associated proteome, we annotated the filtered proteins using Protein Atlas[39,40]. We found that 223 of
143 952 transmembrane proteins (Fig. S2A) and 84 of 336 plasma membrane proteins (Fig. S2B) are
144 annotated as transporters. These trans-membrane proteins mediate the transfer of ions, small
145 molecules, and macromolecules across membranes[41], thus suggesting the potential implication of the
146 HGF-c-MET-MAP4K4 axis in maintaining ion homeostasis of MB cells, and in transferring nutrients and
147 drugs across the PM. Dysregulation of influx or efflux mechanisms can lead to chemotherapy sensitivity
148 or resistance in cancer cells[42,43]. We detected altered PM association of transporters including
149 SLC29A1, SLC4A7 and LRRC8A, where contribution to the influx/efflux of standard chemotherapy
150 cytotoxic drugs has been described[31-32,44-45]. Depletion of MAP4K4 prevented the reduced PM-
151 association of these transporters after HGF stimulation (Fig. S2C). The differences in PM association
152 are not the consequences of altered regulation of gene expression (Fig. S1B). We hence tested the
153 susceptibilities of the cells to cytotoxic drugs by comparing dose-response curves for Lomustine[46] and
154 Etoposide[47] of sgCTL and sgMAP4K4 cells. Under normal growth conditions (10% FBS), depletion of

155 MAP4K4 did not significantly impact the sensitivity of DAOY cells to Etoposide (IC50 value of 3.2 μM
156 and 2.8 μM respectively) or Lomustine (IC50 value of 46.2 μM and 39.5 μM respectively) (Fig. S2D).
157 We additionally tested drug response in cells maintained first in low serum media for 24h (1% FBS) and
158 then treated the cells for 48h with HGF in combination with Lomustine or Etoposide. Under these
159 conditions, depletion of MAP4K4 caused some reduction in Lomustine sensitivity (Fig. S2E). We
160 observed no impact on the response to Etoposide treatment. Taken together, these results suggest a
161 weak sensitizing effect of MAP4K4 towards Lomustine.

162

163 **MAP4K4 controls PM-association of ion transport proteins and prevents cell hyperpolarization**
164 **in HGF-stimulated cells**

165 We furthermore detected MAP4K4-dependent PM association of the chloride channel CLIC1 in
166 HGF-stimulated cells (Fig. 2A, S2F). CLIC1 contributes to MB proliferation *in vitro*, and CLIC1 depletion
167 in MB tumor cell lines significantly reduces tumor cell growth *in vivo*[37]. Gene expression analysis of
168 several MB patient sample cohorts shows CLIC1 overexpression in the tumor samples compared to
169 control tissues (Fig. 2B). Importantly, this elevated CLIC1 expression is associated with worse
170 outcomes in SHH-alpha and Gr4 MB tumors (Fig. 2C). In control cells, PM association of CLIC1 remains
171 unaltered by HGF stimulation. In contrast, HGF stimulation of MAP4K4-depleted cells caused a
172 significant drop of CLIC1 PM association (Fig 2A), suggesting that MAP4K4 is either necessary for
173 CLIC1 transfer to or maintenance at the PM in growth factor-stimulated cells. Conversely, the PM-
174 association of the acetyl-CoA transporter SLC33A1, the $H^+/Ca2^+/Mn2^+$ exchanger TMEM165, the $H^+/K^+$
175 transporter ATPase ATP12A, the sodium bicarbonate co-transporter SLC4A7, the acetyl-CoA
176 transporter SLC19A1 and the Na+/K+ transporter ATP1A3 is significantly increased in MAP4K4-
177 depleted cells stimulated with HGF (Fig. 2D). Using RT-qPCR we found no evidence that MAP4K4
178 depletion altered the mRNA expression of a selection of proteins identified in our study, indicating that
179 altered PM-association is not the consequence of altered transcriptional control (Fig. S1B).

180 To investigate the significance of this HGF- and MAP4K4-dependent modulation of PM
181 localization of ion channels in MB cell ion homeostasis, we performed whole-cell patch-clamp
182 measurement of the electrical properties of sgCTL and sgMAP4K4 DAOY cells. Under starved
183 conditions, MAP4K4 depletion led to an increased whole-cell current compared to control cells (Fig.

184 2E). As we observed the most striking differences in PM association between sgCTL and sgMAP4K4
185 cells after HGF stimulation, we quantified the resting membrane potential ($V_{mem}$) under these conditions.
186 We found that HGF stimulation caused hyperpolarization of MAP4K4-depleted compared to control
187 cells (Fig. 2F). This last finding is in accordance with a more depolarized $V_{mem}$ in disseminating cancer
188 cells, where hyperpolarization leads to a loss of metastatic potential[48].

189 Taken together, these data indicated the implication of MAP4K4 in modulating PM association
190 of ion transport proteins in growth factor-stimulated cells and that one consequence of this MAP4K4
191 function is to prevent hyperpolarization after HGF stimulation.

192

193 **Reduced PM association of CD155 correlates with reduced invasion and motility of MB cells**

194 We found differential PM association of the adhesion and immune-modulatory proteins CD155
195 and CD276 (Fig. 1F). CD276 impacts colorectal cancer cell migration through the Jak2/Stat3/MMP-9
196 signaling pathway[38]. CD155, also referred to as poliovirus receptor (PVR), is a member of the nectin-
197 like family of proteins that can interact with integrins or RTKs and increases FAK, Ras, or RAP1
198 downstream signaling[49]. CD155 is involved in cell adhesion, migration, proliferation, or immune
199 regulation[33], and it is often upregulated in tumors compared to healthy tissues[49]. This renders CD155
200 particularly interesting in the context of tumor progression, where it could contribute to immune evasion
201 and dissemination.

202 HGF stimulation in sgMAP4K4 cells causes reduced PM abundance of CD155 compared to
203 sgCTL cells (Fig. 3A). Decreased PM association of CD155 in MAP4K4 depleted cells is not the result
204 of transcriptional control of *CD155* (Fig. 3B) or reduced protein expression (S1E,H). HGF stimulation
205 rather increased mRNA expression of CD155 both in sgCTL and sgMAP4K4 cells by 10 – 20% (Fig.
206 3B), excluding the possibility that the decrease in CD155 PM association in HGF-stimulated sgMAP4K4
207 is a consequence of transcriptional repression. Combined these findings indicated that MAP4K4 is
208 either required for the transfer or the maintenance of CD155 at the PM under conditions that trigger
209 membrane dynamics and endocytic turnover.

210 To test the requirement of CD155 for HGF-induced collagen invasion, we performed a spheroid
211 invasion assay (SIA)[50,51] (Fig. 3C) using CD155-depleted DAOY cells (Fig. S1H). We found that the
212 reduction of CD155 expression stalled HGF-induced collagen I invasion. To corroborate the implication

213 of CD155 in migration control with another cell line, we tested the effect of CD155 depletion on collagen
214 I invasion in ONS-76 SHH MB cells. These cells invade collagen I independently of exogenous growth
215 factor stimulation. We first confirmed CD155 depletion by siRNA using FACS (Fig. 3D). We then found
216 that CD155 depletion significantly reduced collagen I invasion (Fig. 3E) and that it also reduced
217 proliferation of ONS-76 cells grown as spheroids in 3D cultures (Fig. S3A) without inducing cell death
218 (Fig. S3B). As the inhibition of proliferation by Mitomycin C did not block collagen I invasion in ONS-76
219 cells (Fig. S3C), we concluded that the reduced disseminated cell count in the collagen invasion
220 analysis of CD155-depleted cells is not primarily a consequence of reduced proliferation, but rather of
221 a reduced migratory potential of these cells. To further test this possibility, we assessed the
222 consequence of reduced CD155 expression on motility parameters more directly by single-cell analysis
223 of CD155-depleted ONS-76 cells seeded on collagen I coated plates. Cell movements were recorded
224 by time-lapse video microscopy for five hours. CD155 depletion reduced the average speed of ONS-76
225 cells by 50% (Fig 3F). Phenotypically, cells with decreased CD155 expression displayed increased
226 circularity, increased area, and increased width to length ratio (Fig 3F). Taken together, these data
227 identified the CD155 cell adhesion molecule as a promotor of proliferation, motility, and invasiveness in
228 SHH MB cell models.

229

230 **CD155 is necessary for cerebellar tissue infiltration**

231 To assess whether CD155 depletion prevented cerebellar tissue infiltration and growth of MB
232 cells, we implanted ONS-76-LA-EGFP tumor spheroids onto cerebellar slices and determined growth
233 and invasion after tumor-cerebellar slice co-culture[52]. After 48 hours of co-culture, ONS-76-LA-EGFP
234 cells transfected with siCTL displayed sheet-like infiltration of the surrounding brain tissue (Fig. 3G). In
235 contrast, spheroids of cells transfected with siCD155 did display a much-reduced invasive behavior and
236 remained clustered at the site of initial spheroid positioning. As an indirect measurand for tumor growth
237 and invasion, we quantified the volume of the tumor cell clusters. We observed a ~2-fold reduction of
238 the cluster volume in siCD155 transfected compared to siCTL cells (Fig. 3G, S3D). Some cells in the
239 siCD155 condition still display an invasive phenotype (Fig, 3G, S3D), possibly due to variations in
240 transfection efficiency at the single-cell level. We also evaluated tumor cell proliferation in the tissue-
241 embedded tumor cell clusters using EdU incorporation. We found that depletion of CD155 caused a
242 significant decrease in the number of proliferative cells in the *ex vivo* model, indicating that CD155 also

243 contributes to proliferation in the tissue context (Fig. 3G, S3D). Together, these findings demonstrate
244 that the cell adhesion receptor CD155 contributes to tissue invasion and growth in SHH MB cells.

245

246 **Increased expression of MAP4K4 and EndoA1 in SHH MB**

247 MAP4K4 is overexpressed in MB patient tumor samples[14] and gene expression profiling of 763
248 primary MB samples[53] revealed that *MAP4K4* expression correlates positively with genes involved in
249 endocytosis control (Fig. S4A). Interestingly, the strongest positive correlate with MAP4K4 expression
250 among the endocytosis-regulating genes is *SH3GL2* (EndoA1, r = 0.501), while expression of both
251 *CLTB* (r = - 0.228) and *CLTC* (r = - 0.228) correlate negatively with *MAP4K4* (Fig. S4B). The highest
252 positive correlation between *SH3GL2* and *MAP4K4* expression is observed in SHH MB tumors, where
253 also *CLTC* and *SH3GL2* expression correlate negatively (r=-0.144) (Fig. 4A). Thus, decreased cell
254 migration and altered surface proteome composition in MAP4K4-depleted cells could be
255 mechanistically linked to a clathrin-independent mechanism of endocytosis downstream of HGF-c-MET
256 signaling. A recent genomic and proteomic analysis of a cohort of 218 pediatric brain tumors[54] revealed
257 increased levels of MAP4K4, EndoA1, and EndoA3 – both at protein and RNA levels – but not of
258 EndoA2, in primary MB and ganglioglioma tumor samples (Fig. S4C). These findings highlight high
259 expression of endophilins in MB compared to other central nervous system tumors and pointed towards
260 a potential importance of fast-endophilin-mediated endocytosis (FEME[21]) in this tumor type.

261

262 **MAP4K4 controls PM association and subcellular distribution of FEME regulators**

263 To explore whether MAP4K4 could be involved in PM localization of FEME components such
264 as CIN85/SH3KBP1, CIP4, BIN1 and FBP17, four regulators of FEME priming[55], we compared their
265 abundance in the different surface proteome samples we generated (Tables 1 & 2). We found that HGF
266 stimulation caused a small increase in PM association of these proteins and of EndoA2 in control cells
267 (Fig. 4B). In contrast, PM association of CIN85/SH3KBP1, CIP4, BIN1 and EndoA2 decreased
268 significantly in HGF-stimulated sgMAP4K4 cells, indicating that MAP4K4 controls membrane
269 association of these proteins in cells with activated c-MET. We could not detect EndoA1 and EndoA3
270 in pour proteomic samples. CIN85/SH3KBP1, CIP4 and FNBP1/FBP17 are considered critical
271 mediators of FEME by priming the PM for endophilin A clustering[55]. PM enrichment of these proteins in

272 a MAP4K4-dependent manner in HGF-stimulated cells could thus indicate a link between MAP4K4 and
273 FEME priming. In cells, CIP4 is detectable associated with dotted and filamentous structures that do
274 not co-localize with F-actin (Fig. 4C, D). The depletion of MAP4K4 alters the subcellular localization of
275 CIP4 and causes CIP4 to accumulate in circular patches near cellular protrusions (Fig. 4D). Depletion
276 of EndoA1 phenocopies CIP4 accumulation in these patches (Fig. 4D). Interestingly, we also observed
277 the early endosome marker EEA1 in similar patches in control but not in MAP4K4-or EndoA1-depleted
278 cells (Fig. S5). Whereas this potential colocalization remains to be further investigated, we observed
279 that depletion of EndoA1 or MAP4K4 led to a 20% reduction of EEA1 puncta per cell in a HGF
280 stimulation-independent manner. This indicates that both EndoA1 and MAP4K4 enable formation of
281 early endosomes and further corroborate the shared functionality of the two proteins in endocytosis
282 regulation. Together, these results indicate the implication of MAP4K4 in membrane recruitment,
283 cortical localization and organization of key regulators of FEME in HGF stimulated cells, thereby
284 possibly facilitating an effective FEME sequence[55] (Fig. 4E).

285

286 **EndoA family proteins are required for cell motility and tissue invasion**

287 To determine whether endocytosis pathways (Fig. S6A) are involved in HGF-induced migration
288 control, we assessed the contributions of endocytic pathway components to the HGF-induced invasive
289 phenotype. We used 25 siRNAs targeting 16 essential components of 8 different endocytic pathways
290 (Fig. S6B). Downregulation efficacy of the siRNAs was confirmed by RT-qPCR (Fig. S6C) and HGF
291 induced transwell migration assessed using Boyden chamber assays (Fig. 5A). Consistent with
292 previous studies[13,14], HGF stimulation increased the number of transmigrated cells (~ 2.7-fold increase).
293 Depletion of dynamin 1 and 2 (DNM1 and DNM2) abrogated HGF-induced migration (Fig. 5A),
294 confirming a general role of endocytosis in migration control. Interestingly, depletion of Endophilin A
295 proteins completely abrogated (SH3GL2/EndoA1) or drastically reduced (SH3GL1/EndoA2 and
296 SH3GL3/EndoA3) HGF-induced cell migration (Fig. 5A). In contrast, depletion of clathrin or caveolin,
297 two essential components of endocytic pathways for GF signaling[56], did not prevent or reduce HGF-
298 induced DAOY cell migration. Similarly, depletion of two regulators of micropinocytosis, CTBP1 and
299 RAC1[57], did also not block HGF-induced migration. Both non-transfected and siCTL transfected cells
300 showed similar levels of proliferation up to 72 hours, while depletion of SH3GL1/2/3 and DNM1 exhibited
301 even moderately increased levels of proliferation (Fig. S6D). These data exclude a proliferation defect

302 as the underlying cause of reduced transwell migration in siSH3GL1/2/3- or siDNM1-transfected cells
303 and indicate the implication of EndoA1 and DNM1 in cell migration control.

304

305 **Endophilin A1 is required for 3D collagen I matrix invasion**

306 We next tested whether depletion of EndoA1, DNM1, or clathrin heavy chain (CLTC) also
307 affects 3D collagen I invasiveness of MB cells (Fig. 5B, S6E, F). HGF caused a robust increase in the
308 number of cells disseminating into the collagen I matrix and increased the distance of invasion (~ 6.8-
309 fold increase compared to untreated control). Depletion of EndoA1 or DNM1 significantly reduced HGF-
310 induced collagen I invasion, whereas depletion of CLTC had no effect, indicating that EndoA1 functions
311 in clathrin-independent endocytosis. Consistent with a conserved role of EndoA1 in migration control,
312 depletion of EndoA1 also reduced (~ 1.6-fold decrease) collagen I invasion of ONS-76 cells (Fig. 5C).
313 Depletion of MAP4K4 caused also some, albeit insignificant, reduction in EndoA1 expression (Fig.
314 S6F). To determine whether a compensatory mechanism mediated by EndoA2 or EndoA3[24] may be
315 active in our cell model, we depleted all Endophilin-A proteins simultaneously (TKD). We found that
316 endophilin TKD abrogates HGF-induced cell migration in DAOY cells moderately more effectively than
317 siEndoA1 alone (Fig. 5D). We concluded that EndoA2 or EndoA3 contribute to migration control in MB
318 cells, and that EndoA1 is the most relevant Endophilin in our cell model. In conclusion, we found that
319 EndoA1 mediates a migratory phenotype in MB cells, possibly through a mechanism involving clathrin-
320 independent endocytosis.

321

322 **Endophilin-A1 depletion reduces tissue invasion**

323 We next assessed the role of EndoA1 in tumor growth and invasion control in the tissue context
324 with tumor-cerebellar slice co-culture experiments using ONS-76-LA-EGFP cells. Depletion of EndoA1
325 markedly reduced cerebellum tissue infiltration and prevented the formation of streams of invading cells,
326 which are highly characteristic for this type of MB tumor cell (Fig. 5E, panel a). Individual EndoA1-
327 depleted tumor cells still displayed invasion at the border of the spheres. However, the morphology of
328 these cells appeared more rounded, less mesenchymal compared to control cells (Fig. 5, panel b).
329 Although morphology of the collectivity of the invading cells varied between samples, the considerably
330 reduced invasiveness of EndoA1-depleted cells was apparent (Fig. 5E, S6G), while proliferation was

331 not significantly affected *in vitro* (Fig. S6D) and *ex vivo* (Fig. 5E). Taken together, these data indicate
332 that EndoA1 contributes to the invasive behavior of the tumor cells in the cerebellar tissue without
333 affecting proliferation.

334

335 **Discussion**

336 We found that HGF-induced c-MET activation alters the abundance of transmembrane and
337 plasma membrane-associated proteins in MB cells. The abundance of many of these proteins is
338 reduced by HGF-c-MET activation, indicating either HGF-dependent internalization or attenuated
339 recycling of PM-associated proteins. HGF-induced changes in PM association are increased in
340 MAP4K4-depleted cells and significantly different to control cells for a number of these proteins.
341 Proteins belonging to this group of MAP4K4-regulated proteins are the adhesion receptor CD155 and
342 regulators of fast-endophilin-mediated endocytosis. We show that CD155 can contribute to the
343 oncogenic functions of the MB tumor cells by enabling migration, proliferation and tumor cell growth in
344 the brain tissue. We furthermore identified the fast-endophilin-mediated endocytosis effector protein
345 EndoA1 as a mediator for HGF-induced collagen invasion *in vitro* and for tissue invasion *ex vivo*. The
346 implication of MAP4K4 in PM association of regulators, effectors and targets of endocytic turnover
347 provides a novel conceptual basis for strategies to target the oncogenic phenotype of MB and other
348 RTK-driven solid tumors.

349 PM-associated proteins were enriched by biotin labeling prior to mass-spectrometry analysis.
350 This methodology is expected to label predominately extracellularly bound or anchored proteins,
351 transmembrane proteins, and proteins associated with endocytic vesicles. However, internalized biotin
352 may also lead to the purification of intracellular proteins not normally associated with the plasma
353 membrane. To exclude non-PM proteins, we either used the TMHMM algorithm to predict
354 transmembrane domains in proteins[29] or a data-based filtering approach, yielding two datasets. Former
355 detects surface proteins. However, it also predicts transmembrane domains of proteins associated with
356 other membrane compartments such as the Golgi or ER membranes. The data-based filtering approach
357 selects proteins based on published subcellular localization[30]. This approach is not specifically enriching
358 for proteins with transmembrane domains, and it may include non-PM proteins complexed with PM-
359 associated proteins. The TMHMM and data-based annotation approach selected 21% and 8% of all

360 proteins detected in the initial MS analyses, respectively. The TMHMM approach was highly efficient
361 for determining MAP4K4 impact on PM-association of transporters and channels, which all contain a
362 TM domain. The data-based annotation approach allows for the comparative analysis of the variations
363 in PM association in all the conditions tested using pathway enrichment analysis.

364 MAP4K4 implication in HGF-induced internalization of membrane transport proteins and drug
365 transporters[31] indicated a potential therapeutic benefit of targeting this function of MAP4K4 during
366 chemotherapy, which remains one of the first-line treatments for cancer patients. We hypothesized that
367 indirect modulation of drug uptake or extrusion mechanisms could improve drug efficacy. MAP4K4
368 depletion moderately decreased the sensitivity of DAOY cells to Lomustine, but it had no effect on
369 etoposide treatment efficacy. Although of potential interest, our data are inconclusive and
370 susceptibilities to additional chemotherapeutic drugs such as cisplatin, which is internalized through
371 LRRC8A[58], should be tested in MAP4K4 depleted cells. Consistent with a potential implication of
372 MAP4K4 in sensitization of tumor cells to chemotherapy, MAP4K4 was recently found to reduce the
373 sensitivity of cervical cancer cells to cisplatin treatment via an autophagy-controlled mechanism[59]. The
374 disturbed cell-surface localization of ion channels and transporters could also modify the overall ion
375 homeostasis of the cell. This notion is supported by the subtle alterations in electrical currents we
376 observed in MAP4K4-depleted cells, and it is consistent with previous studies that demonstrated altered
377 electrical conductance properties in tumors compared to healthy tissues[37,60,61]. We found several ion
378 channels susceptible to MAP4K4 regulation and observed an increased current in MAP4K4-depleted
379 cells, together indicating indirect MAP4K4 control of ion homeostasis via regulated ion channel
380 distribution. The lowered potential in MAP4K4-depleted cells after HGF stimulation could be the
381 consequence of a reduced influx of cations, increased efflux of cations, or increased influx of anions.
382 We observed increased PM-association of potassium channels and potassium transport-associated
383 molecules including the P-type cation transporter ATP12A, the $Ca^{2+}$-dependent channels ATP1A3 and
384 KCNMA1 in MAP4K4-depleted cells after HGF stimulation. Thus, MAP4K4 could maintain optimal
385 polarization in HGF-stimulated cells by controlling potassium efflux rates through regulating PM-
386 association of $K^+$ transporters. However, whether differential PM association of potassium channels
387 and de-regulated potassium fluxes are at the origin of the electrical disbalance observed in MAP4K4-
388 depleted cells and contribute to the MAP4K4-associated pro-migratory phenotype remains to be
389 determined.

390 PM-association of CD155 is reduced in MAP4K4-depleted cells that are stimulated with HGF.
391 In glioma cells, CD155 mediates adhesion to the extracellular matrix protein vitronectin, promotes FA
392 turnover and FA signaling towards SRC, paxillin and p130CAS, and thereby contributes to tissue
393 invasion[62]**.** MAP4K4 contributes to FAK activation at the leading edge of migrating cells[14], and our data
394 herein indicate a possibly indirect regulation of this process via the control of CD155 surface expression.
395 Our observation of a more rounded, less mesenchymal morphology in CD155-depleted cells has been
396 described previously in glioma cells[14], and studies in triple-negative aggressive breast cancer cells
397 demonstrated CD155 contribution to the mesenchymal cell state[63]. Depletion of CD155 in these cells
398 triggered mesenchymal to epithelial transition and repressed migration and invasion *in vitro* and *in vivo*.,
399 suggesting that CD155 expression in MB cells could also contribute to migration control indirectly via
400 transcriptional reprogramming. CD155 also represents an attractive therapeutic target due to its ability
401 to inhibit NK cell and $CD8^+$ T-cell activity, thereby contributing to immune evasion of tumor cells[64,65].
402 Kinase-controlled modulation of CD155 surface expression - as we found herein – could enable this
403 process as rather the abundance, and not the absolute absence or presence, of CD155 at the surface
404 of the cell is critical for its immunomodulatory capabilities[49]. Under physiological conditions, CD155 is
405 expressed at low levels, where a balance between its immune activating and inhibitory functions
406 maintains the normal function of immune cells. Thus, the MAP4K4-dependent maintenance of surface
407 expression of CD155 on growth factor-activated cells could not only affect the migratory potential of the
408 cells but also locally (in the tumor microenvironment) repress immune system activation.

409 Our findings point towards a role of fast-endophilin-mediated endocytosis (FEME) through
410 EndoA1 in the control of the invasive phenotype of MB cells. EndoA1 and A3 are highly expressed in
411 SHH MB compared to other brain tumors and their expression correlates positively with MAP4K4 in this
412 tumor type. This contrasts with clathrin, which correlates negatively with MAP4K4 in SHH MB and with
413 the lack of clear evidence that clathrin-mediated endocytosis is necessary for migration control in our
414 cell models. The role of endophilins in cancer progression is complex and controversial, as endophilins
415 can both promote and reduce cancer cell migration, depending on tumor type[24,55,66]. We previously
416 found that 5-(*N*-ethyl-*N*-isopropyl)amiloride (EIPA), a micropinocytosis inhibitor[67], blocks HGF-induced
417 invasion[14]. However, depletion of RAC1 or CTBP1, two upstream activators of micropinocytosis, did
418 not significantly impact HGF-induced motility. This suggests that the pronounced effect of EIPA could
419 be due to the endocytosis-unrelated effects of this drug on ion transport, intracellular pH and

420 cytoskeleton regulation, thus affecting FEME indirectly[24,55]. FEME is involved in the endocytosis of
421 activated receptors at the leading edge of migrating cells[68] and fast and ultrafast endocytosis are
422 important for chemotaxis[69]. FEME could be involved in the internalization of c-MET, thereby controlling
423 signal transmission and persistence of this receptor[24]. Our study identified a possible link between
424 MAP4K4 function and FEME through the regulated PM-association of the FEME priming factors
425 SH3KBP1, CIP4 and FBP17. The observation that MAP4K4 regulates CIP4 PM-association and its
426 accumulation in cortical patches provides circumstantial evidence of spatial regulation of CIP4 by
427 MAP4K4. The early endosome marker EEA1 also localizes to these patches, and it is thus possible that
428 one aspect of FEME processing towards early endosomes occurs preferentially there. Depletion of
429 MAP4K4 prevented EEA1 recruitment to these patches, led to an overall decrease in EEA1-positive
430 vesicles and caused accumulation of CIP4 in this location instead. These phenomena are quite exactly
431 phenocopied by EndoA1 depletion. It is thus possible that MAP4K4 controls FEME by orchestrating a
432 step between FEME priming and trafficking towards early endosomes. Our working model is that
433 MAP4K4 orchestrates PM association of CIP4 from a non-PM-associated subcellular compartment to
434 the “CIP4 patch” in close proximity of or associated with the PM, where also early endosomes enrich.
435 Upon HGF stimulation, CIP4 translocates to the PM, where it is rapidly turned over through EndoA1-
436 dependent FEME before it is recycled back to the PM. Without MAP4K4 function, CIP4 remains
437 associated with the patches, hence the overall amount of PM associated CIP4 increases. Some key
438 questions remain: (i) Does the MAP4K4-dependent mechanism of action involve phosphorylation of
439 one of the components involved in FEME, (ii) is MAP4K4 regulation of CIP4 involved in CIP4-dependent
440 recruitment of Endophilin-A1 to the plasma membrane and (iii) does MAP4K4 control of FEME priming
441 involve the activation of CDC42 downstream of GEFs and GAPs. Elucidation of these mechanisms will
442 be essential to explore therapeutic targeting strategies for specifically repressing MAP4K4 controlled
443 pro-migratory endocytosis.

444 In conclusion, we found that the HGF-c-MET-MAP4K4 axis regulates PM association and
445 surface expression of proteins affecting different pro-oncogenic mechanisms, including chemotherapy
446 sensitivity, ion homeostasis and cell migration and proliferation. Furthermore, our study indicates the
447 contribution of endophilin A proteins in invasion control downstream of MAP4K4. It thus highlights
448 kinase regulation of the PM proteomic composition as a novel mechanism involved in establishing and
449 maintaining the oncogenic phenotype in MB and other solid tumors. The study provides a conceptual

450 basis for further analysis of the dynamic adaptation of tumor cells to environmental cues by plasma
451 membrane proteome modification. Finally, targeting MAP4K4 controlled endocytic activity could
452 represent a novel druggable vulnerability in medulloblastoma cells to restrict tumor growth and
453 dissemination.

454

455 **Materials and Methods**

456

457 **Cell lines and culture conditions**

458 DAOY human MB cells were purchased from the American Type Culture Collection (ATCC, Rockville,
459 MD, USA). ONS-76 cells were generously provided by Michael Taylor (SickKids, Canada). DAOY and
460 DAOY-LA-EGFP cells were cultured in iMEM complemented with 10% FBS. Medium without FBS is
461 used for starvation and further referred to as serum-free medium (SFM). ONS-76-LA-EGFP cells were
462 cultured in RPMI 1640 complemented with 10% FBS. Medium without FBS is used for starvation. DAOY
463 and ONS-76 Lifeact-enhanced green fluorescent protein (LA-EGFP) cells were produced by lentiviral
464 transduction of DAOY cells with pLenti-LA-EGFP. Cell line authentication and cross-contamination
465 testing were performed by Multiplexion GmbH (Heidelberg, Germany) by single nucleotide
466 polymorphism (SNP) profiling.

467

468 **Animals**

469 Pregnant Wild type C57BL/6JRj females were purchased from Janvier Labs and were kept in the animal
470 facilities of the University of Zürich Laboratory Animal Centre. Mouse protocols for organotypic brain
471 slice culture were approved by the Veterinary Office of the Canton Zürich.

472

473 **Generation of CRISPR/Cas9-mediated MAP4K4 knockout cells**

474 MAP4K4 gene-specific single-guide RNA (sgRNA) were designed using Synthego CRISPR design
475 online tool (https://design.synthego.com). Oligos were synthesized by Microsynth (Balgach,
476 Switzerland) and cloned into LentiCRISPRv2 transfer plasmid (Addgene, 52961) with a single tube

477 restriction and ligation method as described by McComb *et al*.[70]. Production of lentiviral vectors and cell
478 transduction was performed as described previously[14]. The efficiency of the knockouts was tested by
479 immunoblot. Only the guide with the highest efficiency has been selected for further experiments
480 (sgMAP4K4#1, exon 7, GGGCGGAGAAATACGTTCAT).

481

482 **Cell-surface labelling**

483 DAOY cells were prepared in four T75 flasks to reach a 70% confluency (per condition and replicates).
484 Standard medium was then replaced with SFM. After 24 hours, cells were 85% confluent, and media
485 were replaced with either pre-warmed SFM or pre-warmed SFM supplemented with 20 ng/mL HGF
486 (PeproTech, 100-39) for 30 min. EZ-Link-Sulfo-NHS-SS-biotin kit (Thermo Scientific, 89881) was used
487 to surface label DAOY_sgCTL and DAOY_sgMAP4K4 cells. In brief, 10 ml EZ-Link-Sulfo-NHS-SS (0.25
488 mg/ml, diluted in ice-cold PBS) was added at 4°C for 30 minutes. Biotinylation reaction was terminated
489 by addition 500 µl of provided quenching solution. Cells from four T75 were collected in a unique tube
490 and washed three times with 10 ml ice-cold TBS (700g, 3 minutes centrifugations). Cell pellets were
491 lysed on ice for 30 minutes with one cycle of sonication (Sonoplus, HD2070) and 5 seconds vortexing
492 every 5 minutes. Insoluble debris pelleted using centrifugation at 10’000 g for 2 minutes. Biotinylated
493 proteins were affinity-purified from lysates using columns containing NeutrAvidin Agarose slurry for one
494 hour at room temperature with end-over-end mixing. After 3 washing steps with lysis buffer, bound
495 proteins were eluted using sample buffer (BioRad, 1610747), complemented with 50 mM DTT, for one
496 hour at room temperature with end-over-end mixing. Purified lysates were kept at -20°C for up to 1 day
497 before Mass spectrometry analysis.

498 Samples were prepared for mass-spectrometry (MS) by using the iST Kit (PreOmics, Germany)
499 according to a modified protocol. In brief, proteins were precipitated with a 10% TCA, solubilized in 50
500 µl iST Kit lysis buffer, boiled at 95°C for 10 minutes and processed with High Intensity Focused
501 Ultrasound (HIFU) for 30 s, with ultrasonic amplitude set to 85%. Proteins were quantified using Qubit,
502 and 50 µg of the samples were for digestion using 50 µl of the iST Kit digestion solution. After 60 min f
503 incubation at 37°C, the digestion was stopped with 100 µl of iST Kit Stop solution. The non-bound
504 components of the solutions in the cartridge were removed by centrifugation at 3800 x g, while the

505 peptides were retained by the iST-filter. Finally, the peptides were washed, eluted, dried and re-
506 solubilized in 20 µl iST Kit LC-Load buffer for MS-Analysis.

507

508 **Liquid chromatography-mass spectrometry analysis**

509 MS analysis was performed on a Q Exactive HF-X mass spectrometer (Thermo Scientific) equipped
510 with a Digital PicoView source (New Objective) and coupled to a M-Class UPLC (Waters). Solvent
511 composition at the two channels was 0.1% formic acid for channel A and 0.1% formic acid, 99.9%
512 acetonitrile for channel B. For each sample, 1 µl of peptides were loaded on a commercial MZ Symmetry
513 C18 Trap Column (100Å, 5 µm, 180 µm x 20 mm, Waters) followed by nanoEase MZ C18 HSS T3
514 Column (100Å, 1.8 µm, 75 µm x 250 mm, Waters). The peptides were eluted at a flow rate of 300 nl/min
515 by a gradient from 8 to 27% B in 85 min, 35% B in 5 min and 80% B in 1 min. Samples were acquired
516 in a randomized order. The mass spectrometer was operated in data-dependent mode (DDA), acquiring
517 a full-scan MS spectrum (350−1'400 m/z) at a resolution of 120'000 at 200 m/z after accumulation to a
518 target value of 3'000'000, followed by HCD (higher-energy collision dissociation) fragmentation on the
519 twenty most intense signals per cycle. HCD spectra were acquired at a resolution of 15'000 using a
520 normalized collision energy of 25 and a maximum injection time of 22 ms. The automatic gain control
521 (AGC) was set to 100'000 ions. Charge state screening was enabled. Singly, unassigned, and charge
522 states higher than seven were rejected. Only precursors with intensity above 110'000 were selected for
523 MS/MS. Precursor masses previously selected for MS/MS measurement were excluded from further
524 selection for 30 s, and the exclusion window was set at 10 ppm. The samples were acquired using
525 internal lock mass calibration on m/z 371.1012 and 445.1200. The mass spectrometry proteomics data
526 were handled using the local laboratory information management system (LIMS)[71]. The mass
527 spectrometry proteomics data have been deposited to the ProteomeXchange Consortium via the
528 PRIDE[72] partner repository with the dataset identifier PXD030597.

529

530 **Protein identification and label-free protein quantification**

531 The acquired raw MS data were processed by MaxQuant (version 1.6.2.3), followed by protein
532 identification using the integrated Andromeda search engine[73]. Spectra were searched against a
533 Swissprot Homo sapiens reference proteome (taxonomy 9606, version from 2016-12-09),

534 concatenated to its reversed decoyed fasta database and common protein contaminants.
535 Carbamidomethylation of cysteine was set as fixed modification, while methionine oxidation and N-
536 terminal protein acetylation were set as variables. Enzyme specificity was set to trypsin/P, allowing a
537 minimal peptide length of 7 amino acids and a maximum of two missed cleavages. MaxQuant Orbitrap
538 default search settings were used. The maximum false discovery rate (FDR) was set to 0.01 for peptides
539 and 0.05 for proteins. Label-free quantification was enabled and a 2-minute window for the match
540 between runs was applied. In the MaxQuant experimental design template, each file is kept separate
541 in the experimental design to obtain individual quantitative values. Protein fold changes were computed
542 based on Intensity values reported in the proteinGroups.txt file. A set of functions implemented in the
543 R package SRMService (http://github.com/protViz/SRMService) was used to filter for proteins with two
544 or more peptides allowing for a maximum of four missing values, and to normalize the data with a
545 modified robust z-score transformation and to compute p-values using the t-test with pooled variance.
546 If all protein measurements are missing in one of the conditions, a pseudo fold change was computed
547 replacing the missing group average by the mean of 10% smallest protein intensities in that condition.
548 For data visualization and normalization across all samples, all group comparison correspond has been
549 processed by statistical analysis of all sgMAP4K4 samples (starved and stimulated) versus all sgCTL
550 samples (starved and stimulated).

551

552 **Chemotherapy sensitivity analysis**

553 400 DAOY sgCTL or sgMAP4K4 were seeded per well in 384 well microplate and incubated 24 hours
554 at 37°C. Media were either replaced with low-serum media (1% FBS) or fresh standard culture media
555 (10% FBS) and incubated for another 24 hours at 37°C. Cells were treated with either low-serum media
556 or low-serum media supplemented with 20 ng/mL HGF (PeproTech, 100-39) or by standard culture
557 media supplemented with Lomustine (Selleckchem, S1840, 5 μM to 100 μM) or Etoposide
558 (Selleckchem, S1225, 1 nM to 10 μM). Cell proliferation was quantified after 48 h of incubation using
559 cell proliferation reagent WST-1 (Roche, 11644807001) following the manufacturer's instructions.
560 Sample absorbance was measured against the background using a microplate reader (Biotek
561 Instruments, Cytation 3) and statistically analyzed using Prism software (GraphPad).

562

563 **Primary tumor gene expression analysis**

564 Gene expression data were obtained from the R2 genomics and visualization platform
565 (https://r2.amc.nl). Berchtold – 172 – MAS5.0 – u133p2; Normal cerebellum – Roth – 9 – MAS5.0 –
566 u133p2; Tumor Medulloblastoma (SHH) – Pfister – 73 – MAS5.0 – u133p2; Tumor Medulloblastoma –
567 Hsieh – 31 – MAS5.0 – u133p2; Tumor Medulloblastoma – Pfister – 273 – MAS5.0 – u133p2; Tumor
568 Medulloblastoma public – Delattre – 57 – MAS5.0 – u133p2; Tumor Medulloblastoma PloS One – Kool
569 – 62 – MAS5.0 – u133p2; Tumor Medulloblastoma – Gilbertson – 76 – MAS5.0 – u133p2 were used to
570 analyze CLIC1 expression in Medulloblastoma versus normal brain tissues. The Tumor
571 Medulloblastoma – Cavalli – 763 – rna_sketch – hugene11t dataset with 763 primary medulloblastoma
572 samples was used for Kaplan Meier survival analysis relative to CLIC1 mRNA expression levels. The
573 Tumor Medulloblastoma – Cavalli – 763 – rna_sketch – hugene11t dataset with 763 primary
574 medulloblastoma samples was used. Molecular pathways correlating with MAP4K4 gene expression
575 have been determine using the R2 genomics and visualization platform built-in KEGG PathwayFinder
576 by Gene correlation tool. Transcriptomic and proteomic data were obtained from the ProTrack pediatric
577 brain tumor database of the Clinical proteomic Tumor Analysis Consortium (CPTAC) and Children's
578 Brain Tumor Tissue Consortium (CBTTC).

579

580 **Patch-clamp analysis**

581 DAOY sgCTL or sgMAP4K4 were seeded in a 35 $mm^2$ dish to reach 20% confluency. After 6 hours of
582 incubation in standard culture condition, the medium was replaced with starvation medium. The next
583 day, cells were treated with either SFM or SFM supplemented with 20 ng/ml HGF for 30 min. Cells were
584 kept in the patch chamber for 30 min. Whole-cell recordings at room temperature were performed on
585 DAOY sgCTL and sgMAP4K4 cells using patch pipettes of ~7 MΩ. The patch pipette solution contained
586 (in mM) 95 K-gluconate, 30 KCl, 4.8 $Na_2HPO_4$, 1.2 $NaH_2PO_4$, 5 glucose, 2.38 $MgCl_2$, 0.76 $CaCl_2$, 1
587 EGTA, 3 K-ATP. The bath solution contained (in mM) 142 NaCl, 1.8 $MgCl_2$, 1.8 $CaCl_2$, 10 HEPES, 3
588 KCl. Compensations and measurements were done within 30 seconds after obtaining whole-cell to
589 avoid drastic changes in cytoplasmic ionic concentration.

590

591 **Gene annotation and pathway enrichment analysis**

592 Gene annotation and pathway enrichment analysis on the surface-proteomics results were performed
593 using the Metascape webtool (https://metascape.org) developed by Zhou *et al.*[39]. Transmembrane
594 proteins were annotated using the TMHMM prediction algorithm[29]. We performed pathway enrichment
595 using all pathway enrichment categories, standard settings and using all proteins identified by mass-
596 spectrometry as background genes.

597

598 **siRNA transfections**

599 100'000 DAOY or ONS-76 cells were seeded per well in 6-well plates. The following day, cells were
600 transfected with 10 nM siRNAs using Lipofectamine RNAiMAX Transfection Reagent (Invitrogen,
601 13778075) plus. siRNA used are referenced in Table S1. After 6 hours, the media were changed, and
602 cells were kept in culture overnight for downstream analyses.

603

604 **RT-qPCR analysis of gene expression**

605 100'000 siRNA transfected DAOY cells (24 h after transfection) were seeded per well in 6 well plates
606 and incubated overnight. For quantitative real-time PCR (RT-qPCR) analysis of target genes, total RNA
607 was isolated using Qiagen Rneasy Mini Kit (Qiagen, 74106). One µg of mRNA was converted to cDNA
608 using the high-capacity cDNA Reverse Transcription Kit (Applied Biosystems, 4368813). RT-qPCR was
609 performed using PowerUp Syber Green (Applied Biosystems, A25776) under conditions optimized for
610 the ABI7900HT instrument. The primers used are referenced in table S2. The ΔΔCT method was used
611 to calculate the relative gene expression of each gene of interest.

612

613 **Flow cytometry analysis of CD155 surface expression**

614 300'000 siRNA transfected DAOY cells were seeded 24h after transfection per well in low adhesion 6
615 well plate (Greiner Bio-one, 657970) and incubated for 6 h in SFM. Cells were then treated with either
616 pre-warmed SFM or SFM supplemented with 20 ng/ml HGF for 30 min. After stimulation, cells were
617 fixed by adding paraformaldehyde pre-warmed to 37°C to a final concentration of 4% and incubated for
618 20 min at 37°C. After one wash with PBS supplemented with 2% FBS, cells were stained with PE-
619 labelled anti-human CD155 (BioLegend, 337610, 1:300), corresponding isotype control antibody

620 (BioLegend, 400114, 1:300), or left unstained for 20 min on ice. Samples were washed with PBS
621 supplemented with 2% FBS, resuspended in PBS and acquired using BD LSRFortessa flow cytometer
622 (BD Bioscience). Fluorescence levels were analyzed using FlowJo software (BD Bioscience).

623

624 **Spheroid invasion assay**

625 2'500 siRNA transfected cells were seeded 24h after transfection per well in 100 µl of standard growth
626 media in cell-repellent 96 well microplates (Greiner Bio-one, 650790). Plates were incubated 24 hours
627 at 37°C in 5% $CO_2$ to allow spheroid formation. 70 µl of culture media were removed from each well
628 and the remaining medium containing the spheroids was complemented with a collagen solution (2.5
629 mg/ml Pure Col Collagen I (Advanced Biomatrix), DMEM 1x (Sigma, D2429) and 0.4% Sodium
630 bicarbonate (Sigma, S8761)). After collagen I polymerization (~ 2 hours), fresh 100 µl SFM +/- HGF 20
631 ng/ml for DAOY spheroids or standard culture media for ONS-76 spheroids was added per well. Cells
632 were incubated at 37°C for 16 hours until fixation with 4% paraformaldehyde. A 1:5000 dilution of
633 Hoechst (Sigma Aldrich, B2883) was added to stain DNA for nuclei visualization. Images of spheroids
634 and invaded cells were acquired on an Operetta CLS High-Content Analysis System (PerkinElmer,
635 HH16000000) at 5x magnification using the Dapi (405 nm) channel. Spheroids were localized in the
636 well by acquiring 3 z-planes with 250 µm z-spacing. Localized spheroids were re-scanned by acquiring
637 16Hoechst-stained z-planes with 25 µm z-spacing and a maximum intensity projection of each spheroid
638 was computed and used for further analysis. Using Harmony software (PerkinElmer), spheroids and
639 invading cells were delineated based on fluorescence threshold. The distance from the center of the
640 spheroid was calculated, and the sum of the cell invasion was determined as the sum of all individual
641 values acquired per well.

642

643 **3D-Cell viability/proliferation (Cell TiterGlo) assay:**

644 Cell viability was determined using CellTiter-Glo® 3D cell viability assay (#G9242, #G9682, Promega).
645 500 siRNA transfected cells/25µL were seeded in U-low adhesion (#4516, Corning) 384-well plate. After
646 48h, the CellTiter-Glo® 3D reagent was added (volume/volume) following the manufacturer's
647 instructions. Plates were incubated at room temperature under agitation for 30 min and luminescence
648 representing the number of viable cells was quantified with a Cytation 3 imaging reader (BioTek®).

649 **Cell proliferation assay**

650 1'000 DAOY cells were seeded in 96 well plates (Greiner Bio-One, 655087). The following day, cells
651 were transfected according to the protocol described above. Six hours after transfection, medium was
652 replaced with serum-free medium. For timepoint 0, WST reagent was added to the corresponding well
653 and incubated 30 min at 37°C. Absorbance at 440 nm was measured using a microplate reader (Biotek
654 Instruments, Cytation 3). 20 ng/ml HGF was added to remaining timepoints and incubated for 24, 48,
655 and 72 hours. At the end of each timepoint, WST reagent was added to the corresponding well and
656 absorbance measured. Each day media was replaced with fresh serum-free medium supplemented
657 with HGF. Changes in absorbance over time were analyzed using Prism 9 software (GraphPad).

658

659 **Single-cell motility assay**

660 1'000 siRNA transfected ONS-76-LA-EGFP cells were seeded in 96 well microplates (Greiner Bio-one,
661 655098) previously coated with Pure Col Collagen I (Advanced BioMatrix, 5005) at 10 $\mu g.cm^{-2}$. After 24
662 h incubation under standard culture conditions, cell motility was acquired using temperature (37°C) and
663 $CO_2$ (5%) controlled Operetta CLS High-Content Analysis System (PerkinElmer, HH16000000) (non-
664 confocal, 20x objective, 4 fields per well, 3 min intervals, 3 h acquisition). Cell segmentation was
665 performed using the LA-EGFP channel. Cell speed, area, circularity, and the width/length ratio were
666 calculated over time using Harmony software (PerkinElmer).

667

668 ***Ex vivo* Organotypic Cerebellum Slice Culture (OCSC)**

669 *Ex vivo* Organotypic Cerebellum Slice Culture was carried out essentially as described previously[56].
670 Wild type C57BL/6JRj mice were sacrificed at postnatal day 8-10. Cerebella were dissected and kept
671 in ice-cold Geys balanced salt solution containing kynurenic acid (GBSSK) and then embedded in 2%
672 low melting point agarose gel. 350 µm thick sections were cut using a vibratome (Leica, VT1200S) and
673 transferred on inserts (Merck Millipore, PICM03050) for further *in vitro* culture. Slices were kept in
674 culture and monitored for 15 days, and media were changed daily for the first week and once in two
675 days thereafter. Spheroids of DAOY-LA-EGFP or ONS-76-LA-EGFP cells transfected with siCTL or
676 CD155 were implanted and then grown in the slices for 48 hours. For HGF stimulation, the feeding
677 medium was supplemented with 20 ng/mL HGF. After treatment, the co-cultured slices were fixed with

678 4% paraformaldehyde and washed three times with PBS. Inserts were incubated in standard cell culture
679 trypsin EDTA and incubated at 37 °C in a humidified incubator for 23 min. After 3 washes, the slices
680 were blocked in PBS containing 3% fetal calf serum, 3% bovine serum albumin (BSA), and 0.3%
681 Triton×100 for 1 hour at room temperature. Primary anti-Calbindin (Abcam, ab108404, 1:1000) and
682 anti-human nuclei (Merck, MAB4383, 1:250) were diluted in the blocking solution and incubated
683 overnight on a shaker at 4°C. Proliferative cells were detected using the Click-iT EdU cell proliferation
684 kit following (Invitrogen, C10340). Unbound primary antibody was removed with 3 washes with PBS
685 supplemented with 3% BSA at RT. Secondary antibodies (Table S3) were incubated for 3 h at RT. The
686 inserts were flat-mounted in glycergel mounting medium (Dako, C0563). Image acquisition was
687 performed on an SP8 Leica confocal microscope (Leica Microsystems) and analyzed using Imaris
688 (Oxford Instruments) and ImageJ (Fiji) software.

689

690 **Immunoblotting (IB)**

691 Immunoblot was carried out as described in[14]. DAOY cells were prepared in 6 well plates to reach 70%
692 confluency within 24 h. Standard media were replaced with SFM. After 24 h at 85% confluency, cells
693 were treated with either SFM or SFM supplemented with 20 ng/ml HGF (PeproTech, 100-39) for 30
694 min. Cells lysis was performed with RIPA buffer for 15 min on ice and cleared lysates were analyzed
695 by SDS-PAGE. Protein concentration was assessed using the Pierce BCA Protein Assay Kit (Thermo
696 Fisher Scientific) according to the manufacturer's instructions. Proteins were separated on Mini-Protean
697 TGX (4-20%) SDS-PAGE gel (Bio-Rad) and transferred to PVDF membranes (Bio-Rad). Following 1 h
698 of blocking with 5% non-fat milk, membranes were probed with primary antibodies listed in
699 Supplementary material (Table S3). GAPDH was used as the internal loading control. HRP-linked
700 secondary antibodies (1:2000) were used to detect the primary antibodies. Chemiluminescence
701 detection was carried out using ChemiDoc Touch Gel imaging system (Bio-Rad). The integrated density
702 of detected bands was quantified using Image Lab software (Bio-Rad).

703

704 **Boyden chamber assay**

705 Transwells with 5 µm pore size (Sarstedt, 83.3932.500) were coated with 0.07 µg/µl Pure Col Collagen
706 I (Advanced BioMatrix, 5005) dissolved in 70% EtOH for a final concentration of 10 $\mu g.cm^{-2}$. 7'500

707 transfected cells (24 h after transfection) were resuspended in serum-free medium and seeded in the
708 upper chamber of a 24 well plate containing the coated transwell. Medium in the lower chamber was
709 either serum-free medium or serum-free medium supplemented with 20 ng/ml HGF (PeproTech, 100-
710 39). Transwell migration was allowed for 18 hours, and cells were then fixed in 4% paraformaldehyde
711 (Thermo Scientific, 28908) in PBS for 10 min. Fixed cells were stained with DAPI for 15 min. The
712 remaining non-invading cells on the upper surface of the membrane were removed using a cotton swab.
713 Images of DAPI-stained nuclei were acquired using an Axio Observer 2 plus fluorescence microscope
714 (Zeiss) at 5x magnification. Nuclei were counted on the membrane areas using ImageJ software and
715 plotted on Prism 9 software (GraphPad).

716

717

718 **Immunofluorescence analysis**

719 1'500 transfected cells (24 h after transfection) were seeded in 384-well plate (Greiner Bio-One,
720 781090) and incubated overnight in normal growth conditions. Cells were starved in low serum condition
721 (1% FBS) for 24 hours and treated with 20 ng/ml HGF for 10- or 30-min. Cells were fixed directly with
722 4% PFA at 37°C for 20 min. Between all subsequent steps, cells were washed five times with PBS
723 using the 50 TS washer (BioTek). Cells were permeabilized with 0.05% saponin for 20 min at RT.
724 Blocking was performed during 1 hour at RT with 1% FBS. Primary antibody (Table S3) solution was
725 added to the sample and shaken at 100 rpm for 2 hours. Secondary antibody (Table S3) solutions were
726 added to the sample and shaken at 100 rpm for 2 hours. Nucleic acids were stained with Hoechst-
727 33342 (Sigma Aldrich, B2883, 1:2000 in PBS) for 20 min at RT. Image acquisition was performed using
728 the Operetta CLS High-Content Analysis System (PerkinElmer, HH16000000) at 40x magnification.
729 Nine fields per well with 9 z-planes with 500 nm z-spacing were acquired per site. Maximum intensity
730 projection was computed and used for subsequent analysis. For puncta quantification, EEA1 or LAMP1
731 signals were segmented using the Harmony software (PerkinElmer) and quantified. The total number
732 of puncta was referred to the number of cells present per field.

733

734 **Statistical analysis**

735 The samples sizes and statistical tests were selected based on previous studies with similar
736 methodologies. Sample sizes were not determined using statistical methods. Statistical analysis was
737 performed using the Prism 9 software (GraphPad). One-way ANOVA repeated measures test using
738 Tukey's multiple comparison was performed for multiple comparisons. P-Value <0.05 were considered
739 significant (* = p<0.05, ** = p<0.01, *** = p<0.001, **** = p<0.0001, ns = not significant).

740

741 **Data availability**

742 The mass spectrometry proteomics data have been deposited to the ProteomeXchange Consortium
743 via the PRIDE[72] partner repository with the dataset identifier PXD030597.

744

745 **Author Contributions**

746 C.C. and M.B. designed the study, prepared the figures, and wrote the manuscript (conceptualization,
747 data curation, formal analysis, visualization, writing). C.C. planned the and conducted the majority of
748 the experiments (investigation, methodology). J.M. generated the CRISPR-Cas9 MAP4K4 cells,
749 conducted the SIA analysis with mitomycin C and generated samples and provided experimental
750 support for *ex vivo* experiments (investigation, methodology). L.R. performed siRNA screening using
751 the Boyden chamber assay (investigation, methodology). M.Z. contributed to the immunofluorescence,
752 FACS and IB sample preparations and analyses (investigation, methodology). D.P. performed the patch
753 clamping experiments (investigation, methodology, visualization) and S.N. contributed to the planning
754 and evaluation of patch clamping experiments (methodology). A.G. generated samples and provided
755 experimental support for *ex vivo* experiments and performed proliferation and viability analyses
756 (investigation, methodology). MB was responsible for supervision and project administration, M.G. and
757 M.B. managed funding acquisition.

758

759 **Acknowledgments**

760 We thank Dr. Paolo Nanni, Dr. Jonas Grossman and Claudia Fortes from the Functional Genomic
761 Center Zürich for their help and support for Mass Spectrometry analysis. We like to thank the UZH
762 electrophysiology facility (e-phac) for their technical support. Imaging was performed with equipment

763 maintained by the Center for Microscopy and Image Analysis, University of Zurich. This study was
764 supported by grants from the Swiss National Science Foundation (SNF_31003A_165860/1,
765 SNF_310030_188793) to MB and from the Childhood Cancer Foundation to MG.

766 **Conflict of interest**

767 The authors have no conflict of interest to declare.

768 **References**

769

770 1. Almén, M. S., Nordström, K. J. V, Fredriksson, R. & Schiöth, H. B. Mapping the human
771 membrane proteome: a majority of the human membrane proteins can be classified according
772 to function and evolutionary origin. *BMC Biol.* **7**, 50 (2009).
773 2. Ye, X., Kaczmarczyk, J. A., Luke, B., Saul, R. G., Whiteley, G. R., Nissley, D. V & Blonder, J.
774 Cell surface protein enrichment for biomarker and drug target discovery using mass
775 spectrometry-based proteomics. in *Proteomic and Metabolomic Approaches to Biomarker*
776 *Discovery* 409–420 (Elsevier, 2020). doi:10.1016/B978-0-12-818607-7.00024-4.
777 3. Orlando, K. & Guo, W. Membrane Organization and Dynamics in Cell Polarity. *Cold Spring Harb.*
778 *Perspect. Biol.* **1**, a001321–a001321 (2009).
779 4. Rodriguez-Furlan, C., Minina, E. A. & Hicks, G. R. Remove, Recycle, Degrade: Regulating
780 Plasma Membrane Protein Accumulation. *Plant Cell* **31**, 2833–2854 (2019).
781 5. Schmid, S. L. Reciprocal regulation of signaling and endocytosis: Implications for the evolving
782 cancer cell. *J. Cell Biol.* **216**, 2623–2632 (2017).
783 6. Hanahan, D. & Weinberg, R. A. Hallmarks of Cancer: The Next Generation. *Cell* **144**, 646–674
784 (2011).
785 7. Mosesson, Y., Mills, G. B. & Yarden, Y. Derailed endocytosis: an emerging feature of cancer.
786 *Nat. Rev. Cancer* **8**, 835–850 (2008).
787 8. Skowron, P., Ramaswamy, V. & Taylor, M. D. Genetic and molecular alterations across
788 medulloblastoma subgroups. *J. Mol. Med.* **93**, 1075–1084 (2015).
789 9. Northcott, P. A., Korshunov, A., Witt, H., Hielscher, T., Eberhart, C. G., Mack, S., Bouffet, E.,
790 Clifford, S. C., Hawkins, C. E., French, P., Rutka, J. T., Pfister, S. & Taylor, M. D.
791 Medulloblastoma comprises four distinct molecular variants. *J. Clin. Oncol.* **29**, 1408–1414

792 (2011).
793 10. Northcott, P. A., Dubuc, A. M., Pfister, S. & Taylor, M. D. Molecular subgroups of
794 medulloblastoma. *Expert Rev. Neurother.* **12**, 871–884 (2012).
795 11. Hovestadt, V., Ayrault, O., Swartling, F. J., Robinson, G. W., Pfister, S. M. & Northcott, P. A.
796 Medulloblastomics revisited: biological and clinical insights from thousands of patients. *Nat. Rev.*
797 *Cancer* **20**, 42–56 (2020).
798 12. Aldape, K. *et al.* Challenges to curing primary brain tumours. *Nat. Rev. Clin. Oncol.* **16**, 509–
799 520 (2019).
800 13. Santhana Kumar, K., Tripolitsioti, D., Ma, M., Grählert, J., Egli, K. B., Fiaschetti, G., Shalaby, T.,
801 Grotzer, M. A. & Baumgartner, M. The Ser/Thr kinase MAP4K4 drives c-Met-induced motility
802 and invasiveness in a cell-based model of SHH medulloblastoma. *Springerplus* **4**, (2015).
803 14. Tripolitsioti, D., Kumar, K. S., Neve, A., Migliavacca, J., Capdeville, C., Rushing, E. J., Ma, M.,
804 Kijima, N., Sharma, A., Pruschy, M., McComb, S., Taylor, M. D., Grotzer, M. A. & Baumgartner,
805 M. MAP4K4 controlled integrin β1 activation and c-Met endocytosis are associated with invasive
806 behavior of medulloblastoma cells. *Oncotarget* **9**, (2018).
807 15. Hood, J. D. & Cheresh, D. A. Role of integrins in cell invasion and migration. *Nat. Rev. Cancer*
808 **2**, 91–100 (2002).
809 16. de Franceschi, N., Hamidi, H., Alanko, J., Sahgal, P. & Ivaska, J. Integrin traffic-the update. *J.*
810 *Cell Sci.* **128**, 839–852 (2015).
811 17. Kermorgant, S., Zicha, D. & Parker, P. J. PKC controls HGF-dependent c-Met traffic, signalling
812 and cell migration. *EMBO J.* **23**, 3721–3734 (2004).
813 18. Alanko, J., Mai, A., Jacquemet, G., Schauer, K., Kaukonen, R., Saari, M., Goud, B. & Ivaska, J.
814 Integrin endosomal signalling suppresses anoikis. *Nat. Cell Biol.* **17**, 1412–1421 (2015).
815 19. Kjaerulff, O., Brodin, L. & Jung, A. The Structure and Function of Endophilin Proteins. *Cell*
816 *Biochem. Biophys.* **60**, 137–154 (2011).
817 20. Masuda, M., Takeda, S., Sone, M., Ohki, T., Mori, H., Kamioka, Y. & Mochizuki, N. Endophilin
818 BAR domain drives membrane curvature by two newly identified structure-based mechanisms.
819 *EMBO J.* **25**, 2889–2897 (2006).
820 21. Ferreira, A. P. A. & Boucrot, E. Mechanisms of Carrier Formation during Clathrin-Independent
821 Endocytosis. *Trends Cell Biol.* **28**, 188–200 (2018).

822 22. Verstreken, P., Kjaerulff, O., Lloyd, T. E., Atkinson, R., Zhou, Y., Meinertzhagen, I. A. & Bellen,
823 H. J. Endophilin Mutations Block Clathrin-Mediated Endocytosis but Not Neurotransmitter
824 Release. *Cell* **109**, 101–112 (2002).
825 23. Gad, H., Ringstad, N., Löw, P., Kjaerulff, O., Gustafsson, J., Wenk, M., Di Paolo, G., Nemoto,
826 Y., Crum, J., Ellisman, M. H., De Camilli, P., Shupliakov, O. & Brodin, L. Fission and Uncoating
827 of Synaptic Clathrin-Coated Vesicles Are Perturbed by Disruption of Interactions with the SH3
828 Domain of Endophilin. *Neuron* **27**, 301–312 (2000).
829 24. Boucrot, E., Ferreira, A. P. A., Almeida-Souza, L., Debard, S., Vallis, Y., Howard, G., Bertot, L.,
830 Sauvonnet, N. & McMahon, H. T. Endophilin marks and controls a clathrin-independent
831 endocytic pathway. *Nature* **517**, 460–465 (2015).
832 25. Genet, G., Boyé, K., Mathivet, T., Ola, R., Zhang, F., Dubrac, A., Li, J., Genet, N., Henrique
833 Geraldo, L., Benedetti, L., Künzel, S., Pibouin-Fragner, L., Thomas, J.-L. & Eichmann, A.
834 Endophilin-A2 dependent VEGFR2 endocytosis promotes sprouting angiogenesis. *Nat.*
835 *Commun.* **10**, 2350 (2019).
836 26. Poudel, K. R., Roh-Johnson, M., Su, A., Ho, T., Mathsyaraja, H., Anderson, S., Grady, W. M.,
837 Moens, C. B., Conacci-Sorrell, M., Eisenman, R. N. & Bai, J. Competition between TIAM1 and
838 Membranes Balances Endophilin A3 Activity in Cancer Metastasis. *Dev. Cell* **45**, 738--752.e6
839 (2018).
840 27. Giachino, C., Lantelme, E., Lanzetti, L., Saccone, S., Valle, G. Della & Migone, N. A Novel SH3-
841 Containing Human Gene Family Preferentially Expressed in the Central Nervous System.
842 *Genomics* **41**, 427–434 (1997).
843 28. Itzhak, D. N., Davies, C., Tyanova, S., Mishra, A., Williamson, J., Antrobus, R., Cox, J., Weekes,
844 M. P. & Borner, G. H. H. A Mass Spectrometry-Based Approach for Mapping Protein Subcellular
845 Localization Reveals the Spatial Proteome of Mouse Primary Neurons. *Cell Rep.* **20**, 2706–2718
846 (2017).
847 29. Moller, S., Croning, M. D. R. & Apweiler, R. Evaluation of methods for the prediction of
848 membrane spanning regions. *Bioinformatics* **17**, 646–653 (2001).
849 30. Itzhak, D. N., Tyanova, S., Cox, J. & Borner, G. H. Global, quantitative and dynamic mapping of
850 protein subcellular localization. *Elife* **5**, 1–36 (2016).
851 31. Huang, Y., Anderle, P., Bussey, K. J., Barbacioru, C., Shankavaram, U., Dai, Z., Reinhold, W.

852 C., Papp, A., Weinstein, J. N. & Sadée, W. Membrane transporters and channels: Role of the
853 transportome in cancer chemosensitivity and chemoresistance. *Cancer Res.* **64**, 4294–4301
854 (2004).
855 32. Rubino, S., Bach, M. D., Schober, A. L., Lambert, I. H. & Mongin, A. A. Downregulation of
856 leucine-rich repeat-containing 8A limits proliferation and increases sensitivity of glioblastoma to
857 temozolomide and carmustine. *Front. Oncol.* **8**, 1–12 (2018).
858 33. Gao, J., Zheng, Q., Xin, N., Wang, W. & Zhao, C. CD155, an onco-immunologic molecule in
859 human tumors. *Cancer Sci.* **108**, 1934–1938 (2017).
860 34. Picarda, E., Ohaegbulam, K. C. & Zang, X. Molecular pathways: Targeting B7-H3 (CD276) for
861 human cancer immunotherapy. *Clin. Cancer Res.* **22**, 3425–3431 (2016).
862 35. Curigliano, G., Criscitiello, C., Gelao, L. & Goldhirsch, A. Molecular pathways: Human leukocyte
863 antigen G(HLA-G). *Clin. Cancer Res.* **19**, 5564–5571 (2013).
864 36. Morishita, K., Watanabe, K. & Ichijo, H. Cell volume regulation in cancer cell migration driven by
865 osmotic water flow. *Cancer Sci.* **110**, 2337–2347 (2019).
866 37. Francisco, M. A. *et al.* Chloride intracellular channel 1 cooperates with potassium channel EAG2
867 to promote medulloblastoma growth. *J. Exp. Med.* **217**, 324–387 (2020).
868 38. Liu, F., Zhang, T., Zou, S., Jiang, B. & Hua, D. B7-H3 promotes cell migration and invasion
869 through the Jak2/Stat3/MMP9 signaling pathway in colorectal cancer. *Mol. Med. Rep.* **12**, 5455–
870 5460 (2015).
871 39. Zhou, Y., Zhou, B., Pache, L., Chang, M., Khodabakhshi, A. H., Tanaseichuk, O., Benner, C. &
872 Chanda, S. K. Metascape provides a biologist-oriented resource for the analysis of systems-
873 level datasets. *Nat. Commun.* **10**, (2019).
874 40. Thul, P. J. *et al.* A subcellular map of the human proteome. *Science (80-. ).* **356**, eaal3321
875 (2017).
876 41. DEFELICE, L. Transporter structure and mechanism. *Trends Neurosci.* **27**, 352–359 (2004).
877 42. Hoffmann, E. K. & Lambert, I. H. Ion channels and transporters in the development of drug
878 resistance in cancer cells. *Philos. Trans. R. Soc. B Biol. Sci.* **369**, 20130109 (2014).
879 43. Giacomini, K. M. *et al.* Membrane transporters in drug development. *Nat. Rev. Drug Discov.* **9**,
880 215–236 (2010).
881 44. Deeley, R. G., Westlake, C. & Cole, S. P. C. Transmembrane Transport of Endo- and

882 Xenobiotics by Mammalian ATP-Binding Cassette Multidrug Resistance Proteins. *Physiol. Rev.*
883 **86**, 849–899 (2006).
884 45. Sørensen, B. H., Nielsen, D., Thorsteinsdottir, U. A., Hoffmann, E. K. & Lambert, I. H.
885 Downregulation of LRRC8A protects human ovarian and alveolar carcinoma cells against
886 Cisplatin-induced expression of p53, MDM2, p21 Waf1/Cip1 , and Caspase-9/-3 activation. *Am.*
887 *J. Physiol. Physiol.* **310**, C857–C873 (2016).
888 46. Packer, R. J. *et al.* Outcome for children with medulloblastoma treated with radiation and
889 cisplatin, CCNU, and vincristine chemotherapy. *J. Neurosurg.* **81**, 690–698 (1994).
890 47. Greenberg, H. S., Chamberlain, M. C., Glantz, M. J. & Wang, S. Adult medulloblastoma:
891 Multiagent chemotherapy. *Neuro. Oncol.* **3**, 29–34 (2001).
892 48. Payne, S. L., Levin, M. & Oudin, M. J. Bioelectric Control of Metastasis in Solid Tumors.
893 *Bioelectricity* **1**, 114–130 (2019).
894 49. Kučan Brlić, P., Lenac Roviš, T., Cinamon, G., Tsukerman, P., Mandelboim, O. & Jonjić, S.
895 Targeting PVR (CD155) and its receptors in anti-tumor therapy. *Cell. Mol. Immunol.* **16**, 40–52
896 (2019).
897 50. Kumar, K. S., Pillong, M., Kunze, J., Burghardt, I., Weller, M., Grotzer, M. A., Schneider, G. &
898 Baumgartner, M. Computer-assisted quantification of motile and invasive capabilities of cancer
899 cells. *Sci. Rep.* **5**, 15338 (2015).
900 51. Roper, S. J., Linke, F., Scotting, P. J. & Coyle, B. 3D spheroid models of paediatric SHH
901 medulloblastoma mimic tumour biology , drug response and metastatic dissemination. *Sci. Rep.*
902 1–17 (2021).
903 52. Neve, A., Kumar, K. S., Tripolitsioti, D., Grotzer, M. A. & Baumgartner, M. Investigation of brain
904 tissue infiltration by medulloblastoma cells in an ex vivo model. *Sci. Rep.* **7**, 1–12 (2017).
905 53. Cavalli, F. M. G. *et al.* Intertumoral Heterogeneity within Medulloblastoma Subgroups. *Cancer*
906 *Cell* **31**, 737--754.e6 (2017).
907 54. Petralia, F. *et al.* Integrated Proteogenomic Characterization across Major Histological Types of
908 Pediatric Brain Cancer. *Cell* **183**, 1962-1985.e31 (2020).
909 55. Casamento, A. & Boucrot, E. Molecular mechanism of Fast Endophilin-Mediated Endocytosis.
910 *Biochem. J.* **477**, 2327–2345 (2020).
911 56. Cendrowski, J., Mamińska, A. & Miaczynska, M. Endocytic regulation of cytokine receptor

912 signaling. *Cytokine Growth Factor Rev.* **32**, 63–73 (2016).
913 57. Liberali, P., Kakkonen, E., Turacchio, G., Valente, C., Spaar, A., Perinetti, G., Böckmann, R. A.,
914 Corda, D., Colanzi, A., Marjomaki, V. & Luini, A. The closure of Pak1-dependent
915 macropinosomes requires the phosphorylation of CtBP1/BARS. *EMBO J.* **27**, 970–981 (2008).
916 58. Sørensen, B. H., Dam, C. S., Stürup, S. & Lambert, I. H. Dual role of LRRC8A-containing
917 transporters on cisplatin resistance in human ovarian cancer cells. *J. Inorg. Biochem.* **160**, 287–
918 295 (2016).
919 59. Huang, H., Han, Q., Zheng, H., Liu, M., Shi, S., Zhang, T., Yang, X., Li, Z., Xu, Q., Guo, H., Lu,
920 F. & Wang, J. MAP4K4 mediates the SOX6-induced autophagy and reduces the
921 chemosensitivity of cervical cancer. *Cell Death Dis.* **13**, (2022).
922 60. Dozmorov, M. G., Hurst, R. E., Culkin, D. J., Kropp, B. P., Frank, M. B., Osban, J., Penning, T.
923 M. & Lin, H.-K. Unique patterns of molecular profiling between human prostate cancer LNCaP
924 and PC-3 cells. *Prostate* **69**, 1077–1090 (2009).
925 61. Pollak, J., Rai, K. G., Funk, C. C., Arora, S., Lee, E., Zhu, J., Price, N. D., Paddison, P. J.,
926 Ramirez, J.-M. & Rostomily, R. C. Ion channel expression patterns in glioblastoma stem cells
927 with functional and therapeutic implications for malignancy. *PLoS One* **12**, e0172884 (2017).
928 62. Sloan, K. E., Stewart, J. K., Treloar, A. F., Matthews, R. T. & Jay, D. G. CD155/PVR enhances
929 glioma cell dispersal by regulating adhesion signaling and focal adhesion dynamics. *Cancer*
930 *Res.* **65**, 10930–10937 (2005).
931 63. Zheng, Q., Gao, J., Yin, P., Wang, W., Wang, B., Li, Y. & Zhao, C. CD155 contributes to the
932 mesenchymal phenotype of triple-negative breast cancer. *Cancer Sci.* **111**, 383–394 (2020).
933 64. Okumura, G., Iguchi-Manaka, A., Murata, R., Yamashita-Kanemaru, Y., Shibuya, A. & Shibuya,
934 K. Tumor-derived soluble CD155 inhibits DNAM-1–mediated antitumor activity of natural killer
935 cells. *J. Exp. Med.* **217**, (2020).
936 65. He, W., Zhang, H., Han, F., Chen, X., Lin, R., Wang, W., Qiu, H., Zhuang, Z., Liao, Q., Zhang,
937 W., Cai, Q., Cui, Y., Jiang, W., Wang, H. & Ke, Z. CD155T/TIGIT Signaling Regulates CD8+ T-
938 cell Metabolism and Promotes Tumor Progression in Human Gastric Cancer. *Cancer Res.* **77**,
939 6375–6388 (2017).
940 66. Behavior, M., Majumdar, S., Gong, E. M., Vizio, D. Di, Dreyfuss, J., Degraff, D. J., Hager, M. H.,
941 Park, P. J., Bellmunt, J., Matusik, R. J., Rosenberg, J. E. & Adam, R. M. Loss of Sh3gl2 /

942 Endophilin A1 Is a Common Event in Urothelial Carcinoma that Promotes. **15**, 749–760 (2013).
943 67. Kabayama, H., Takeuchi, M., Taniguchi, M., Tokushige, N., Kozaki, S., Mizutani, A., Nakamura,
944 T. & Mikoshiba, K. Syntaxin 1B suppresses macropinocytosis and semaphorin 3A-induced
945 growth cone collapse. *J. Neurosci.* **31**, 7357–7364 (2011).
946 68. Mondal, S., Powers, I., Narayan, K., Botterbusch, S. & Baumgart, T. Endophilin Recruitment via
947 GPCR Interactions Enables Membrane Curvature Generation in the Absence of Anionic Lipids.
948 *bioRxiv* 2020.07.11.198937 (2020).
949 69. Watanabe, S. & Boucrot, E. Fast and ultrafast endocytosis. *Curr. Opin. Cell Biol.* **47**, 64–71
950 (2017).
951 70. McComb, S., Aguadé-Gorgorió, J., Harder, L., Marovca, B., Cario, G., Eckert, C., Schrappe, M.,
952 Stanulla, M., Von Stackelberg, A., Bourquin, J. P. & Bornhauser, B. C. Activation of concurrent
953 apoptosis and necroptosis by SMAC mimetics for the treatment of refractory and relapsed ALL.
954 *Sci. Transl. Med.* **8**, (2016).
955 71. Türker, C., Akal, F., Joho, D., Panse, C., Barkow-Oesterreicher, S., Rehrauer, H. & Schlapbach,
956 R. B-Fabric. in *Proceedings of the 13th International Conference on Extending Database*
957 *Technology - EDBT '10* 717 (ACM Press, 2010).
958 72. Perez-Riverol, Y. *et al.* The PRIDE database and related tools and resources in 2019: Improving
959 support for quantification data. *Nucleic Acids Res.* **47**, D442–D450 (2019).
960 73. Cox, J. & Mann, M. MaxQuant enables high peptide identification rates, individualized p.p.b.-
961 range mass accuracies and proteome-wide protein quantification. *Nat. Biotechnol.* **26**, 1367–
962 1372 (2008).
963 74. Falsig, J. & Aguzzi, A. The prion organotypic slice culture assay—POSCA. *Nat. Protoc.* **3**, 555–
964 562 (2008).
965
966

967 **Figure legends**

968 **Figure 1**

969 **HGF-c-MET signaling alters composition of plasma membrane (PM)-associated proteome.**

970 **(A)** General workflow for cell-surface protein isolation, mass spectrometry and computational analysis
971 used. **(B)** Volcano plot of PM-associated proteins identified by deep mass-spectrometry analysis.
972 Colored dots indicate proteins with predicted TM domain (blue, upper) or PM localization (red, lower).
973 sgCTL: CRISPR/CAS-9 control guide RNA expressing cells; sgMAP4K4: CRISPR/CAS-9 MAP4K4-
974 specific guide RNA expressing cells; + HGF: SFM supplemented with 20 ng/ml HGF for 30 min. **(C)**
975 log2 Fold change of RAW, TM or PM protein comparisons between treatments. Green: positive fold
976 change (increased association), red: negative fold change (decreased association). **(D)** Quantification
977 of the PM association of different receptor tyrosine kinases. Box plots display normalized z-score values
978 extracted from all-group comparison of MS analysis. N = 4 independent experiments, min to max, * =
979 p<0.05 (mixed effect analysis, with Šídák's multiple comparisons test). **E)** Heatmaps of enriched
980 ontology clusters across multiple two-group analyses of significantly altered, PM-annotated proteins
981 with positive (upper) or negative (lower) fold change. Panel colors are defined by adjusted p-values.
982 Gray cells: No enrichment detected for that term in the corresponding two-group analyses. Missing
983 comparisons: no enrichment detected **(F)** Overview of a selection of potentially clinically relevant PM-
984 associated proteins (log2 FC >1, adjusted p-values <0.2). Yellow bar: no change; red arrow: decreased
985 PM association; green arrow: increased PM association.

986

987 **Figure 2**

988 **MAP4K4 modulates the ion homeostasis of DAOY cells.**

989 **(A)** Quantification of PM association of CLIC1 by MS. Box plots display normalized z-score values
990 extracted from all-group comparison of MS analysis. N = 4 independent experiments, min to max, ** =
991 adjusted p<0.01 of one-way ANOVA. **(B)** U133P Affymetrix gene chip micro array analysis of CLIC1
992 mRNA expression levels in normal brain tissue and MB tumor samples. **(C)** Kaplan Meier survival
993 analyses in four MB subgroups relative to CLIC1 mRNA expression levels. **(D)** Quantification of PM
994 association of ion transport proteins by MS. Box plots display normalized z-score values extracted from
995 all-group comparison of MS analysis. N = 4 independent experiment, min to max, * = adjusted p<0.05,
996 ** = adjusted p<0.01 of one-way ANOVA. **(E)** Whole cell currents measured at holding potential ranging

997 from −100 mV to +80 mV (in steps of 20 mV) in DAOY cells +/- KO of MAP4K4. N = 13-16 cells
998 measured independently. **F)** Quantification of the membrane potential of DAOY cells +/- KO of MAP4K4
999 and +/- HGF stimulation (20 ng/ml, 30 min) in normal [$Cl^-$] SFM medium. N = 8-16 cells measured
1000 independently.

1001

1002 **Figure 3**

1003 **CD155 promotes migration and invasion.**

1004 **(A)** Quantification of PM association of CD155. Box plots display normalized z-score values extracted
1005 from all-group comparison of MS analysis. N = 4 independent experiments, min to max, * = p<0.05 of
1006 one-way ANOVA. **(B)** RT-qPCR analysis of *CD155* mRNA expression in siCTL and siMAP4K4 -/+ HGF
1007 stimulation (30 min), ** = p<0.01 of one-way ANOVA. **(C)** SIA of siCTL or siCD155 transfected DAOY
1008 cells -/+ HGF stimulation. Left: Representative images of Hoechst-stained nuclei in inverted greyscale
1009 at end point of SIA. Scale bar = 300 µm. Right Box plots display sum of distances of invasion. N = 3
1010 independent experiments, min to max, * = p<0.05, **** = p<0.0001 of one-way ANOVA. **(D)** Surface
1011 expression analysis of CD155 by flow cytometry on ONS-76 cells. Left: Histograms of anti-CD155 PE
1012 intensities. Right: bar diagram depicting mean PE (CD155) intensities in siCD155 relative to siCTL cells
1013 of n = 3 independent experiments, ** = p<0.01 of unpaired t-test. **(E)** SIA of siCTL or siCD155
1014 transfected ONS-76 cells. Left: Representative images of Hoechst-stained nuclei in inverted greyscale.
1015 Scale bar = 300 µm. Right Box plots display sum of distances of invasion. N = 3 independent
1016 experiments. * = p<0.05 of unpaired t-test. **(F)** Single cell motility analysis of siCTL and siCD155
1017 transfected ONS-76 cells. Inverted grey-scale images are representative LA-EGFP fluorescence
1018 images of siRNA transfected DAOY cells seeded on collagen-I coated plates. Scale bar = 25 µm. Speed
1019 and morphological properties of cells were quantified in 5 min intervals for 300 min and are displayed
1020 over time (x/y plots) and averaged (box-dot plots). N = 3 independent experiments, min to max, **** =
1021 p<0.0001 of unpaired t-test, ns = not significant. **(G)** OCSC of siCTL or siCD155 ONS-76 cells implanted
1022 on cerebellar slices for 48h. Left: representative images of OCSCs. Cyan: Human nuclei, magenta:
1023 Calbindin (Purkinje cells), Scale bar: 400 µm. Right: Bar plots show volume and proliferation index of n
1024 = 3 spheroids ** = p<0.01 (unpaired t-test).

1025

1026 **Figure 4**

1027 **MAP4K4 controls CIP4 PM association and subcellular localization.**

1028 **(A**) Two gene analyses of SH3GL2, MAP4K4 and CLTC expression across the four MB subgroups.
1029 Correlation coefficient and adjusted p-values are shown. **(B)** Quantification of PM association of
1030 regulators of FEME priming and endocytosis effectors. Box plots display normalized z-score values
1031 extracted from all-group comparison of MS analysis. N = 4 independent experiments, min to max, * =
1032 p<0.05 of one-way ANOVA. **(C)** Confocal microscopy analysis of endogenous CIP4 localization in siCTL
1033 or siEndoA1 transfected ONS-76 cells. Cyan: LA-EGFP (F-actin), magenta: CIP4, blue: Hoechst (DNA).
1034 **(D)** Confocal microscopy analysis of CIP4 subcellular localization in siCTL, siMAP4K4 and siEndoA1
1035 transfected cells. Magenta: CIP4, blue: Hoechst. **(E)** Model for MAP4K4 regulation of the fast endophilin
1036 mediated endocytosis. Under control conditions, during priming: CIP4 is recruited to the plasma
1037 membrane (PM). PM-associated CIP4 recruits EndoA1 to the plasma membrane. After receptor
1038 activation, endophilins initiate FEME and promote the internalization of the carrier and trafficking
1039 towards early endosomes.

1040

1041 **Figure 5**

1042 **EndoA1 is required for migration and tissue invasion.**

1043 **(A)** Boyden chamber transwell migration assay using siRNA transfected DAOY cells. siRNAs as
1044 indicated. Significance is calculated from the comparison of each individual sample with the HGF-
1045 stimulated siCTL sample. N = 3-4 independent experiments, mean & SD, * = p<0.05, ** = p<0.01, *** =
1046 p<0.001 of one-way ANOVA. **(B)** SIA analysis of EndoA1 implication in collagen I invasion. Left:
1047 Inverted greyscale images of Hoechst-stained nuclei of DAOY spheroids ± HGF (20 ng/ml) at endpoint.
1048 siRNA transfections as indicated. Scale bar = 300 µm. Right: Quantification of the total distance of
1049 invasion as sum of all distances measured from the center of spheroids as shown in A. Each dot
1050 represents 1 spheroid, n = 3 independent experiments, mean & SD, ** = p<0.01, **** = p<0.0001 of
1051 one-way ANOVA. **(C)** Left: Inverted greyscale images of Hoechst-stained nuclei of ONS-76 spheroids
1052 at end point of SIA. Scale bar = 300 µm. Right: Quantification of the invasion as sum of the distances
1053 as in B, * = p<0.05 of unpaired t-test. **(D)** Left: Inverted greyscale images of Hoechst-stained nuclei of
1054 DAOY cells transfected with three siRNAs targeting EndoA1, A2 and A3 (TKD) ± HGF (20 ng/ml) at
1055 end point of SIA. Scale bar = 300 µm. Right: Quantification of the invasion as sum of the distances as
1056 in B, **** = p<0.0001 of one-way ANOVA. Scale bar in all representative images = 300 µm. **(E)** Left:

1057 Maximum intensity projection of representative confocal sections of OCSC implanted with transfected
1058 ONS-76 spheroids 48h after implantation. Cyan: Lifeact-EGFP; Magenta: calbindin (Purkinje cells).
1059 Right: Quantification of tumor volume and proportion of EdU-positive cells/area. N = 3, technical
1060 replicates, mean & SD, * = p<0.05, unpaired t-test. Scale bar = 400 µm. a and b are higher magnification
1061 images of ONS-76 tumor cells at the invasion front. Cyan: Actin cytoskeleton of tumor cells, magenta:
1062 Purkinje cells.
1063

1064 **Graphical abstract:**

1065 c-MET activation upon HGF stimulation induces c-MET internalization and induces downstream
1066 MAP4K4 activity. **(1)** MAP4K4 is required downstream of activated c-MET for the maintenance of
1067 surface presentation of CD155 in activated cells. CD155 expression is required for MB cell migration,
1068 invasion and proliferation in the tissue context. **(2)** MAP4K4 is required downstream of activated c-MET
1069 to maintain membrane depolarization, possibly by regulating the surface localization of several ion
1070 channels and transporters. **(3)** MAP4K4 is required downstream of activated c-MET cause PM-proximal
1071 localization of FEME effector CIP4, FBP17 and CIN85. The FEME effector endophilin A is necessary
1072 for MB cell migration, invasion and dissemination.
1073

1074 **Supplementary figures:**

1075 **Figure S1**

1076 **Validation of gene depletion efficiencies.**

1077 **(A)** Immunoblot analysis of MAP4K4 expression in DAOY sgCTL and sgMAP4K4 cells used in
1078 proteome analysis. Treatments as indicated (HGF 20 ng/ml, 30 min). **(B)** Relative mRNA expression of
1079 a selection of proteins with significantly altered PM association. N = 3 independent experiments, mean
1080 & SD, * = p<0.05, ** = p<0.01, **** = p<0.0001. **(C)** Volcano plots of log2FC versus adjusted p-values
1081 of two-group analyses of all identified proteins. **(D)** Histogram of log2FC and adjusted p-values of two-
1082 group analyses. RAW: All proteins detected, TM: Transmembrane domain-containing proteins, PM:
1083 Plasma membrane-annotated proteins. **(E)** IB analysis of protein expression in sgCTL and sgMAP4K4
1084 cells treated as indicated. **(F)** Volcano plots of log2FC versus adjusted p-values of two-group analyses
1085 of all identified proteins. **(G)** Relative mRNA expression analysis for *CD155* and *CD276* with siRNAs

1086 used. N = 3 independent experiments, mean & SD, * = p<0.05, ** = p<0.01, **** = p<0.0001 of unpaired
1087 t-test. **H)** IB analysis of CD155 expression in siMAP4K4 and siCD155 transfected cells.

1088

1089 **Figure S2**

1090 **MAP4K4 promotes HGF-induced internalization of solute carriers and transporters.**

1091 **(A)** Pie chart representing the proportion of proteins with predicted transmembrane domains (blue).
1092 Proteins annotated as transporters using Protein Atlas are highlight in red. **(B)** Pie chart representing
1093 the proportion of PM-annotaed proteins (blue) in all proteins identified in MS analysis. Proteins
1094 annotated as transporters using Protein Atlas are highlight in red. **(C)** Quantification of the PM-
1095 association of solute carriers and transporters involved in chemotherapy sensitivity and resistance.
1096 Relative z-Score value extracted from all-group comparison. n = 4 independent experiments, min to
1097 max, * = adjusted p<0.05 of one-way ANOVA. **(D)** Dose-response curve and corresponding $IC_{50}$ values
1098 of Lomustine and Etoposide after 48 hours treatment under standard culture conditions (10% FBS). **(E)**
1099 Dose-response curve and corresponding $IC_{50}$ values of Lomustine and Etoposide after 48 hours
1100 treatment +/- HGF stimulation under low-serum culture conditions (1% FBS). n ≥ 3 technical replicates,
1101 mean + SEM. **(F)** Selection of proteins with predicted transmembrane domains with knwon implication
1102 in ion transport. Potential ions involved are indicated. Normalized z-score values extracted from all-
1103 group comparison of MS analysis are depicted. Fold change and p-values extracted from each two-
1104 group analysis are shown. N = 4 independent experiments. Green: upregulated, red: downregulated,
1105 black: unchanged.

1106

1107 **Figure S3**

1108 **CD155 depletion prevents tissue invasion *ex vivo*.**

1109 **(A)** CellTiter Glo proliferation assay of siCTL or siCD155 transfected ONS-76 cells grown as spheroids.
1110 **** = p<0.0001 of unpaired t-test. **(B)** CellTox Green cytotoxicity assay of siCTL or siCD155 transfected
1111 ONS-76 cells grown as spheroids. **** = p<0.0001 of unpaired t-test. **(C)** SIA analysis of ONS-76 cells
1112 treated with mitomycin C, 2 µM for 24h. Upper: Inverted grey scale images of Hoechst-stained nuclei
1113 at end-point. Lower: Quantification of total invasion total distance of invasion. **(D)** Confocal microscopy
1114 analysis of OCSCs two days after implantation of spheroid of DOAY cells transfected with indicated

1115 siRNAs. Cyan: Human nuclei, Magenta: Calbindin (Purkinje cells). Tumor cell area is indicated with
1116 dashed line in inverted gray-scale confocal images. Scale bar = 400 µm.
1117
1118 **Figure S4**
1119 **SH3GL2 is highly expressed in SHH MB tumors and correlates with MAP4K4 expression.**

1120 **(A)** MAP4K4 co-expressed genes from 763 primary medulloblastoma samples were used to interrogate
1121 KEGG pathway database. **(B)** Top 20 genes with a positive (Left) or negative (Right) correlative
1122 expression score with MAP4K4. **(C)** Expression of MAP4K4, SH3GL1, SH3GL2 and SH3GL3 at RNA
1123 and protein levels in 218 pediatric brain tumors across seven histologic types. Copy number variation
1124 (CNV) and mutations are represented if available. The data were obtained from the R2: Genomics
1125 Analysis and Visualization platform (http://r2.amc.nl) and CPTAC data portal (http://pbt.cptac-data-
1126 view.org/).
1127
1128 **Figure S5**
1129 **EndoA1- and MAP4K4-mediated regulation of EEA1.**

1130 Confocal microscopy analysis of the early endosome marker EEA1. Left: Maximum intensity projection
1131 of siCTL, siEndoA1 and siMAP4K4 transfected DAOY cells. Blue: Nucleic acids (Hoechst), Orange:
1132 EEA1. Scale bar = 50 µm. Right: Quantification of the EEA1 positive puncta per cell. N = 4 technical
1133 replicates Min to Max, * $p<0.05$, ** $p<0.01$, *** $p<0.001$, **** $p<0.0001$, ns = not significant (one-way
1134 ANOVA).
1135
1136 **Figure S6**
1137 **Implication of endocytosis on MB tumor progression.**

1138 **(A)** Schematic representation of endocytic pathways in mammalian cells. **(B)** List of target genes used
1139 for siRNA screen and corresponding endocytic pathways. Pathways with dynamin-independent vesicle
1140 closure and abscission are shown in turquoise. **(C)** Depletion efficacy of siRNAs used in transwell
1141 migration screen assessed by RT-qPCR after transfection with the Dharmacon transfection reagent.
1142 RNA extraction occurred at endpoint of Boyden chamber assay. N = 2 to 9 independent experiments,
1143 Mean + SD. **(D)** WST cell proliferation analysis . N = 2 independent experiments, Mean + SEM. **(E)**

1144 Depletion efficacy of siRNAs against EndoA1, DNM1 and CLTC1 assessed by RT-qPCR with the
1145 Invitrogen transfection reagent. RNA extraction occurred at endpoint of SIA. N = 6 independent
1146 experiments, Mean + SD, **** p<0.0001. **(F)** Immunoblot (left and middle panels) and RT-qPCR
1147 analysis (right panel) of siRNA-mediated Endophilin-A1 depletion in ONS-76 cells. Quantification of RT-
1148 qPCR analysis: N = 3 independent experiments, Mean + SD. ** p<0.01, ns = not significant. **(G)**
1149 Confocal microscopy analysis of OCSCs two days after implantation of spheroid of DOAY cells
1150 transfected with indicated siRNAs. Cyan: LA-EGFP, Magenta: Calbindin (Purkinje cells).

1151

1152 **Supplementary files**

1153 **Table 1 | Surface Proteome Transmembrane prediction TMHMM filtering**

1154 Excel File: Table 1_SurfaceProteome_TransMembraneAnnotation-TMHMM-Filtering_Capdeville2021

1155 **Table 2 | Surface Proteome Plasma membrane annotation filtering**

1156 Excel File: Table 2_SurfaceProteome_PlasmaMembraneAssociation_Capdeville2021

1157 **Table 3 | Significant fold change for Transmembrane predicted proteins**

1158 Excel File: Table 3_Significant_FoldChange_TransMembraneAnnotation_Capdeville2021

1159 **Table 4 | Significant fold change for Plasma membrane annotated proteins**

1160 Excel File: Table 4_Significant_FoldChange_PlasmaMembraneAssociation_Capdeville2021

1161 **Tables S1-S3**

1162 Antibodies and primer lists

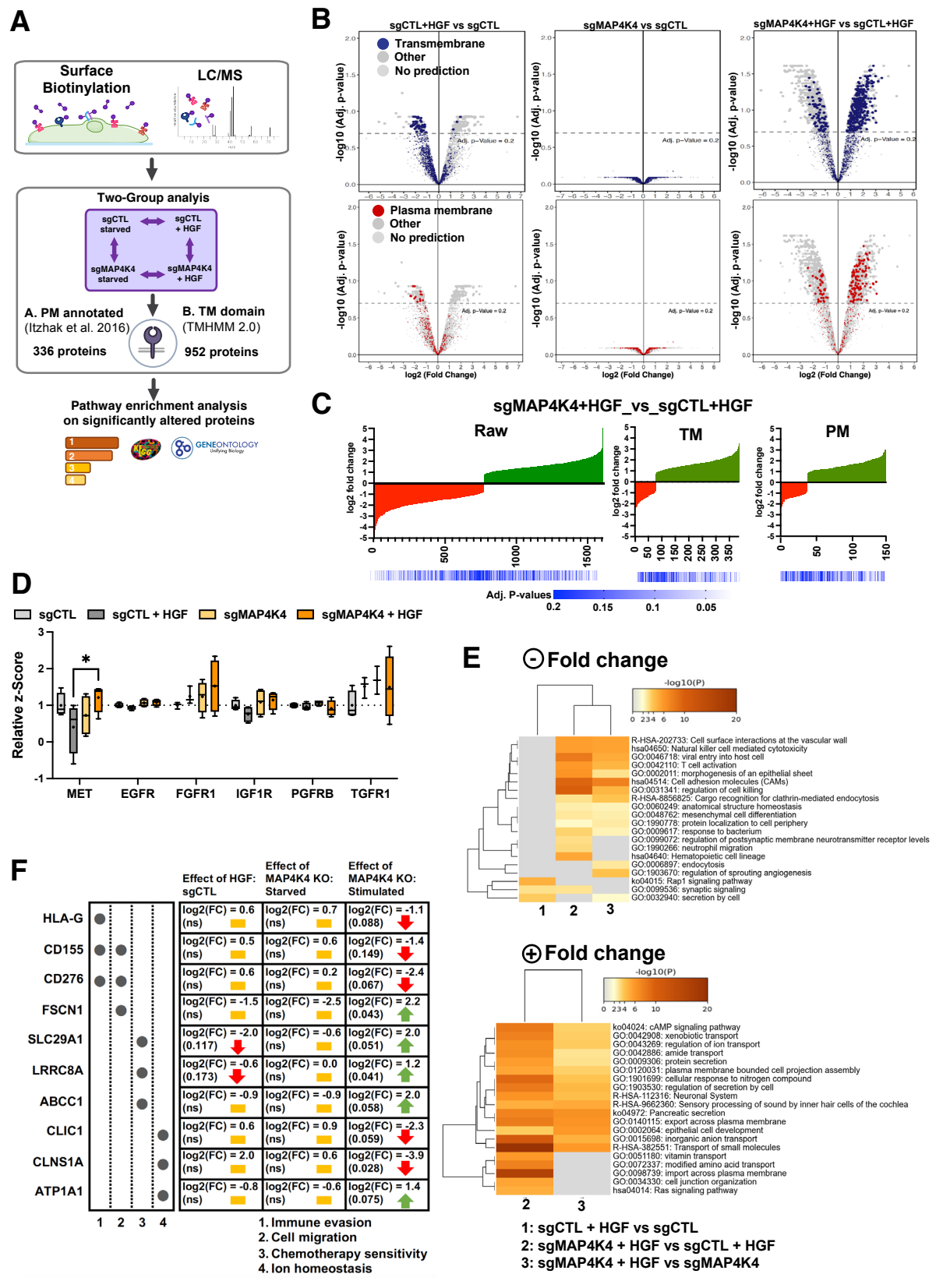
A
Surface Biotinylation
LC/MS
Two-Group analysis
sgCTL starved
sgCTL + HGF
sgMAP4K4 starved
sgMAP4K4 + HGF
A. PM annotated
(Itzhak et al. 2016)
336 proteins
B. TM domain
(TMHMM 2.0)
952 proteins
Pathway enrichment analysis
on significantly altered proteins
GENEONTOLOGY
Unifying Biology
B
sgCTL+HGF vs sgCTL
sgMAP4K4 vs sgCTL
sgMAP4K4+HGF vs sgCTL+HGF
Transmembrane
Other
No prediction
Plasma membrane
Other
No prediction
-log10 (Adj. p-value)
log2 (Fold Change)
Adj. p-Value = 0.2
C
sgMAP4K4+HGF_vs_sgCTL+HGF
Raw
TM
PM
log2 fold change
Adj. P-values
0.2
0.15
0.1
0.05
D
sgCTL
sgCTL + HGF
sgMAP4K4
sgMAP4K4 + HGF
Relative z-Score
MET
EGFR
FGFR1
IGF1R
PGFRB
TGFR1
E
Fold change
-log10(P)
R-HSA-202733: Cell surface interactions at the vascular wall
hsa04650: Natural killer cell mediated cytotoxicity
GO:0046718: viral entry into host cell
GO:0042110: T cell activation
GO:0002011: morphogenesis of an epithelial sheet
hsa04514: Cell adhesion molecules (CAMs)
GO:0031341: regulation of cell killing
R-HSA-8856825: Cargo recognition for clathrin-mediated endocytosis
GO:0060249: anatomical structure homeostasis
GO:0048762: mesenchymal cell differentiation
GO:1990778: protein localization to cell periphery
GO:0009617: response to bacterium
GO:0099072: regulation of postsynaptic membrane neurotransmitter receptor levels
GO:1990266: neutrophil migration
hsa04640: Hematopoietic cell lineage
GO:0006897: endocytosis
GO:1903670: regulation of sprouting angiogenesis
ko04015: Rap1 signaling pathway
GO:0099536: synaptic signaling
GO:0032940: secretion by cell
Fold change
ko04024: cAMP signaling pathway
GO:0042908: xenobiotic transport
GO:0043269: regulation of ion transport
GO:0042886: amide transport
GO:0009306: protein secretion
GO:0120031: plasma membrane bounded cell projection assembly
GO:1901699: cellular response to nitrogen compound
GO:1903530: regulation of secretion by cell
R-HSA-112316: Neuronal System
R-HSA-9662360: Sensory processing of sound by inner hair cells of the cochlea
ko04972: Pancreatic secretion
GO:0140115: export across plasma membrane
GO:0002064: epithelial cell development
GO:0015698: inorganic anion transport
R-HSA-382551: Transport of small molecules
GO:0051180: vitamin transport
GO:0072337: modified amino acid transport
GO:0098739: import across plasma membrane
GO:0034330: cell junction organization
hsa04014: Ras signaling pathway
1: sgCTL + HGF vs sgCTL
2: sgMAP4K4 + HGF vs sgCTL + HGF
3: sgMAP4K4 + HGF vs sgMAP4K4
F
Effect of HGF: sgCTL
Effect of MAP4K4 KO: Starved
Effect of MAP4K4 KO: Stimulated
HLA-G
CD155
CD276
FSCN1
SLC29A1
LRRC8A
ABCC1
CLIC1
CLNS1A
ATP1A1
log2(FC) = 0.6 (ns)
log2(FC) = 0.7 (ns)
log2(FC) = -1.1 (0.088)
log2(FC) = 0.5 (ns)
log2(FC) = 0.6 (ns)
log2(FC) = -1.4 (0.149)
log2(FC) = 0.6 (ns)
log2(FC) = 0.2 (ns)
log2(FC) = -2.4 (0.067)
log2(FC) = -1.5 (ns)
log2(FC) = -2.5 (ns)
log2(FC) = 2.2 (0.043)
log2(FC) = -2.0 (0.117)
log2(FC) = -0.6 (ns)
log2(FC) = 2.0 (0.051)
log2(FC) = -0.6 (0.173)
log2(FC) = 0.0 (ns)
log2(FC) = 1.2 (0.041)
log2(FC) = -0.9 (ns)
log2(FC) = -0.9 (ns)
log2(FC) = 2.0 (0.058)
log2(FC) = 0.6 (ns)
log2(FC) = 0.9 (ns)
log2(FC) = -2.3 (0.059)
log2(FC) = 2.0 (ns)
log2(FC) = 0.6 (ns)
log2(FC) = -3.9 (0.028)
log2(FC) = -0.8 (ns)
log2(FC) = -0.6 (ns)
log2(FC) = 1.4 (0.075)
1. Immune evasion
2. Cell migration
3. Chemotherapy sensitivity
4. Ion homeostasis

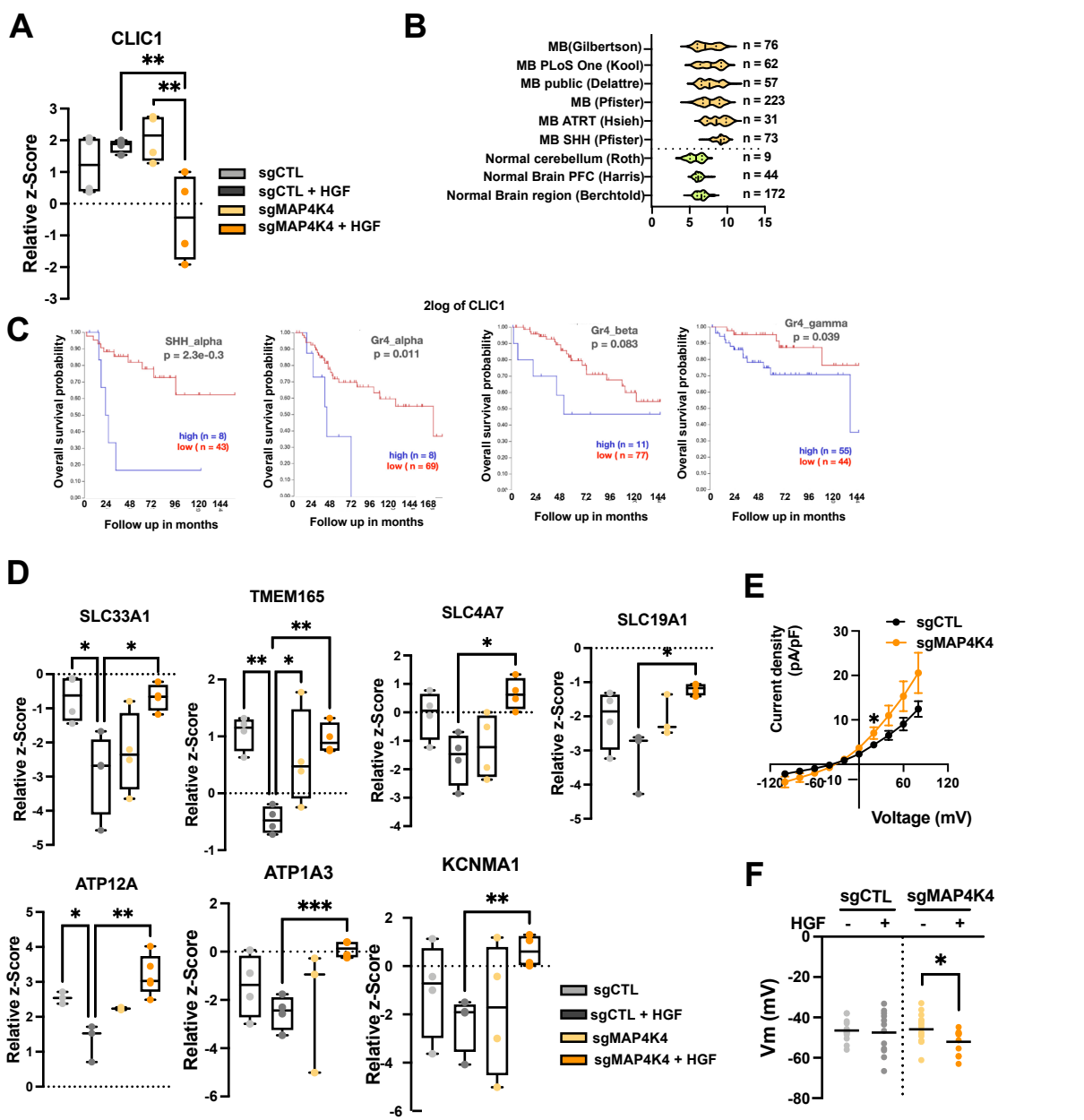
A
CLIC1
Relative z-Score
sgCTL
sgCTL + HGF
sgMAP4K4
sgMAP4K4 + HGF
B
MB(Gilbertson)
MB PLoS One (Kool)
MB public (Delattre)
MB (Pfister)
MB ATRT (Hsieh)
MB SHH (Pfister)
Normal cerebellum (Roth)
Normal Brain PFC (Harris)
Normal Brain region (Berchtold)
n = 76
n = 62
n = 57
n = 223
n = 31
n = 73
n = 9
n = 44
n = 172
2log of CLIC1
C
SHH_alpha
p = 2.3e-0.3
high (n = 8)
low ( n = 43)
Gr4_alpha
p = 0.011
high (n = 8)
low ( n = 69)
Gr4_beta
p = 0.083
high (n = 11)
low ( n = 77)
Gr4_gamma
p = 0.039
high (n = 55)
low ( n = 44)
Overall survival probability
Follow up in months
D
SLC33A1
TMEM165
SLC4A7
SLC19A1
ATP12A
ATP1A3
KCNMA1
Relative z-Score
sgCTL
sgCTL + HGF
sgMAP4K4
sgMAP4K4 + HGF
E
sgCTL
sgMAP4K4
Current density (pA/pF)
Voltage (mV)
F
sgCTL
sgMAP4K4
HGF
Vm (mV)

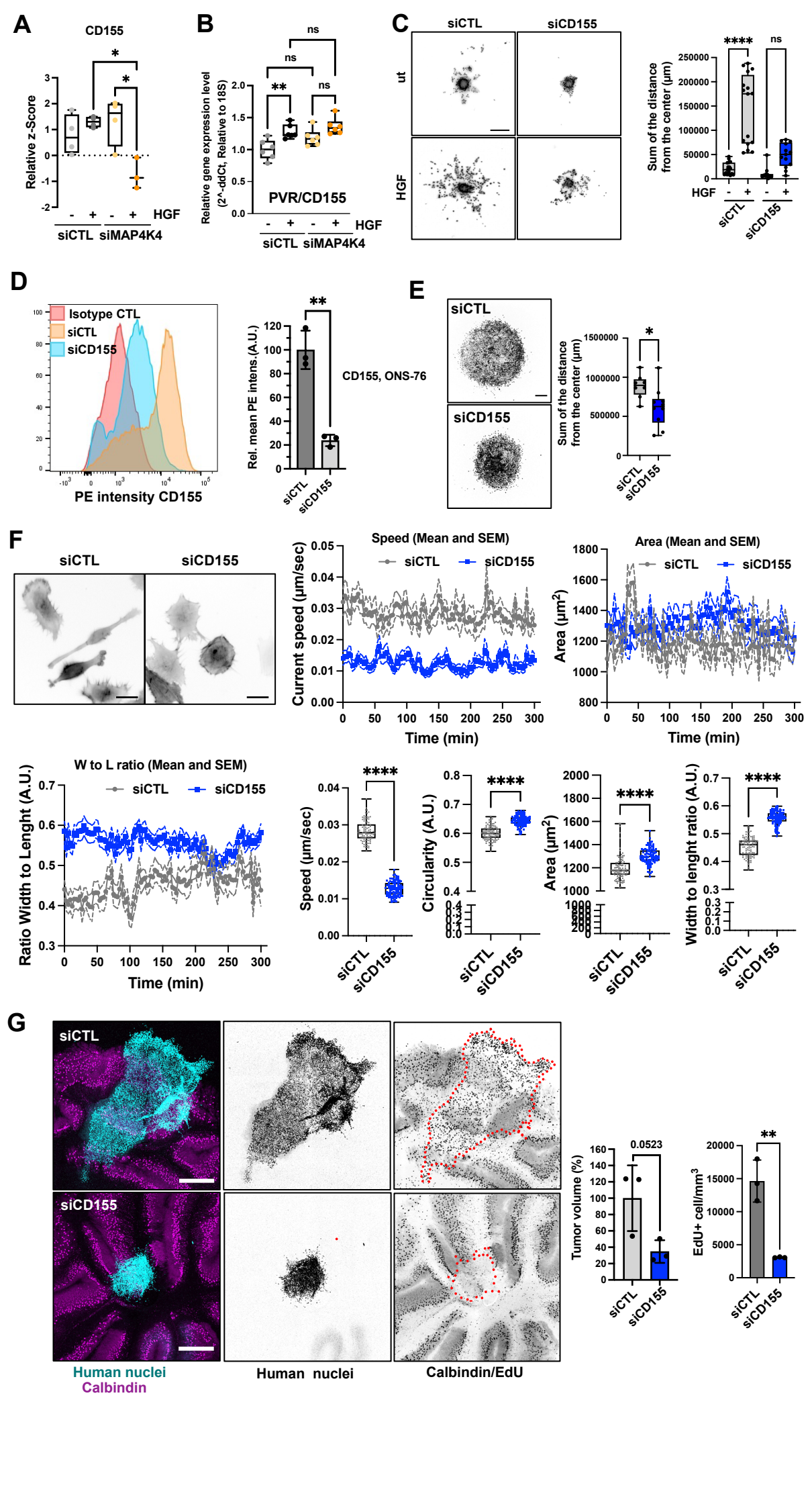
A
CD155
Relative z-Score
HGF
siCTL siMAP4K4
B
PVR/CD155
Relative gene expression level (2^-ddCt, Relative to 18S)
HGF
siCTL siMAP4K4
C
siCTL
siCD155
ut
HGF
Sum of the distance from the center (µm)
HGF
siCTL
siCD155
D
Isotype CTL
siCTL
siCD155
PE intensity CD155
Rel. mean PE intens.(A.U.)
CD155, ONS-76
siCTL
siCD155
E
siCTL
siCD155
Sum of the distance from the center (µm)
siCTL
siCD155
F
siCTL
siCD155
Speed (Mean and SEM)
Current speed (µm/sec)
Time (min)
Area (Mean and SEM)
Area (µm²)
Time (min)
W to L ratio (Mean and SEM)
Ratio Width to Lenght (A.U.)
Time (min)
Speed (µm/sec)
Circularity (A.U.)
Area (µm²)
Width to lenght ratio (A.U.)
siCTL
siCD155
G
siCTL
siCD155
Human nuclei
Calbindin
Human nuclei
Calbindin/EdU
Tumor volume (%)
0.0523
EdU+ cell/mm³
siCTL
siCD155

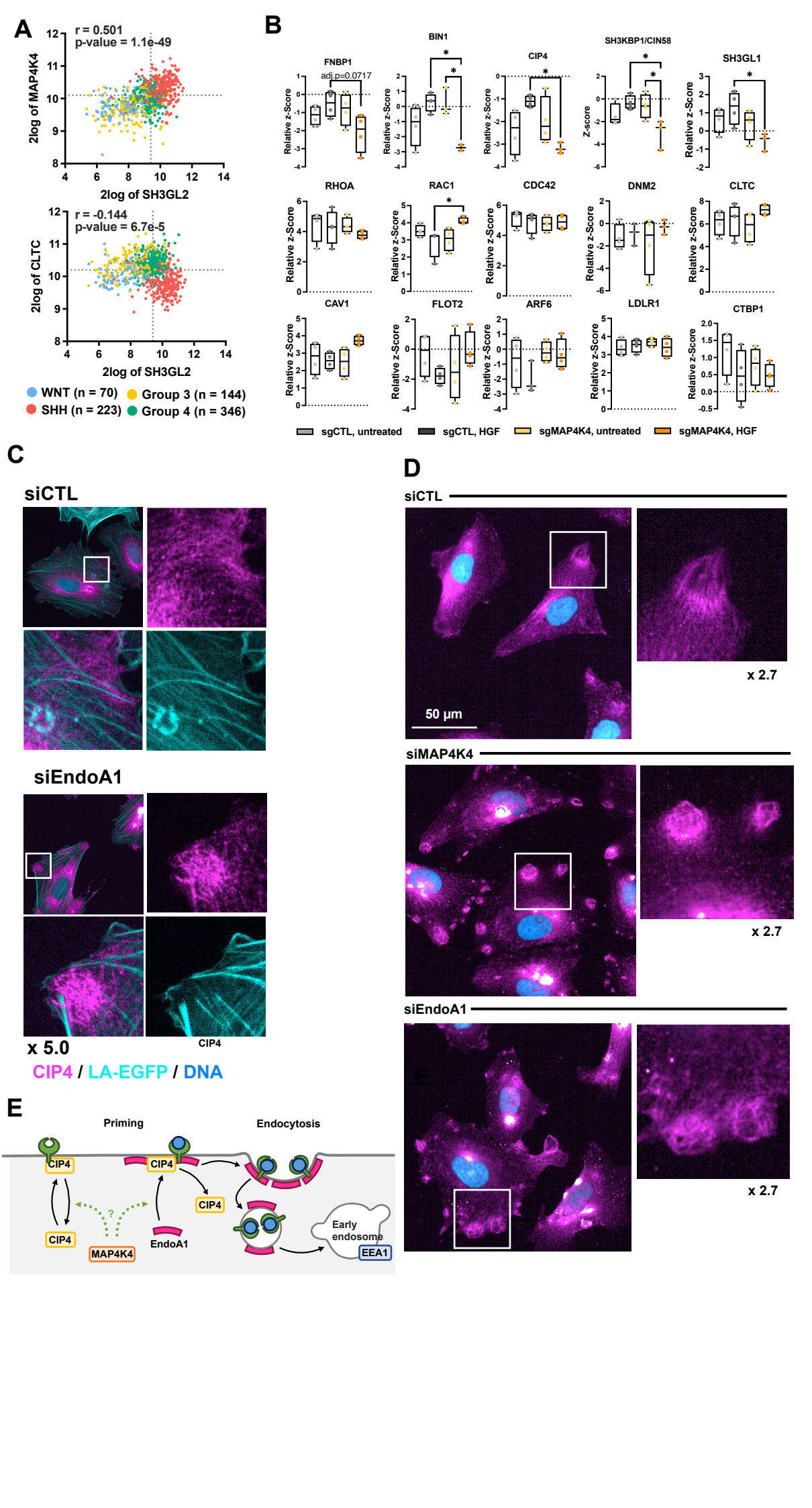
A
r = 0.501
p-value = 1.1e-49
2log of MAP4K4
2log of SH3GL2
r = -0.144
p-value = 6.7e-5
2log of CLTC
2log of SH3GL2
WNT (n = 70)
SHH (n = 223)
Group 3 (n = 144)
Group 4 (n = 346)
B
FNBP1
adj.p=0.0717
BIN1
CIP4
SH3KBP1/CIN58
SH3GL1
RHOA
RAC1
CDC42
DNM2
CLTC
CAV1
FLOT2
ARF6
LDLR1
CTBP1
Relative z-Score
Z-score
sgCTL, untreated
sgCTL, HGF
sgMAP4K4, untreated
sgMAP4K4, HGF
C
siCTL
siEndoA1
x 5.0
CIP4
CIP4 / LA-EGFP / DNA
D
siCTL
50 µm
x 2.7
siMAP4K4
x 2.7
siEndoA1
x 2.7
E
Priming
Endocytosis
CIP4
CIP4
CIP4
CIP4
MAP4K4
EndoA1
Early endosome
EEA1

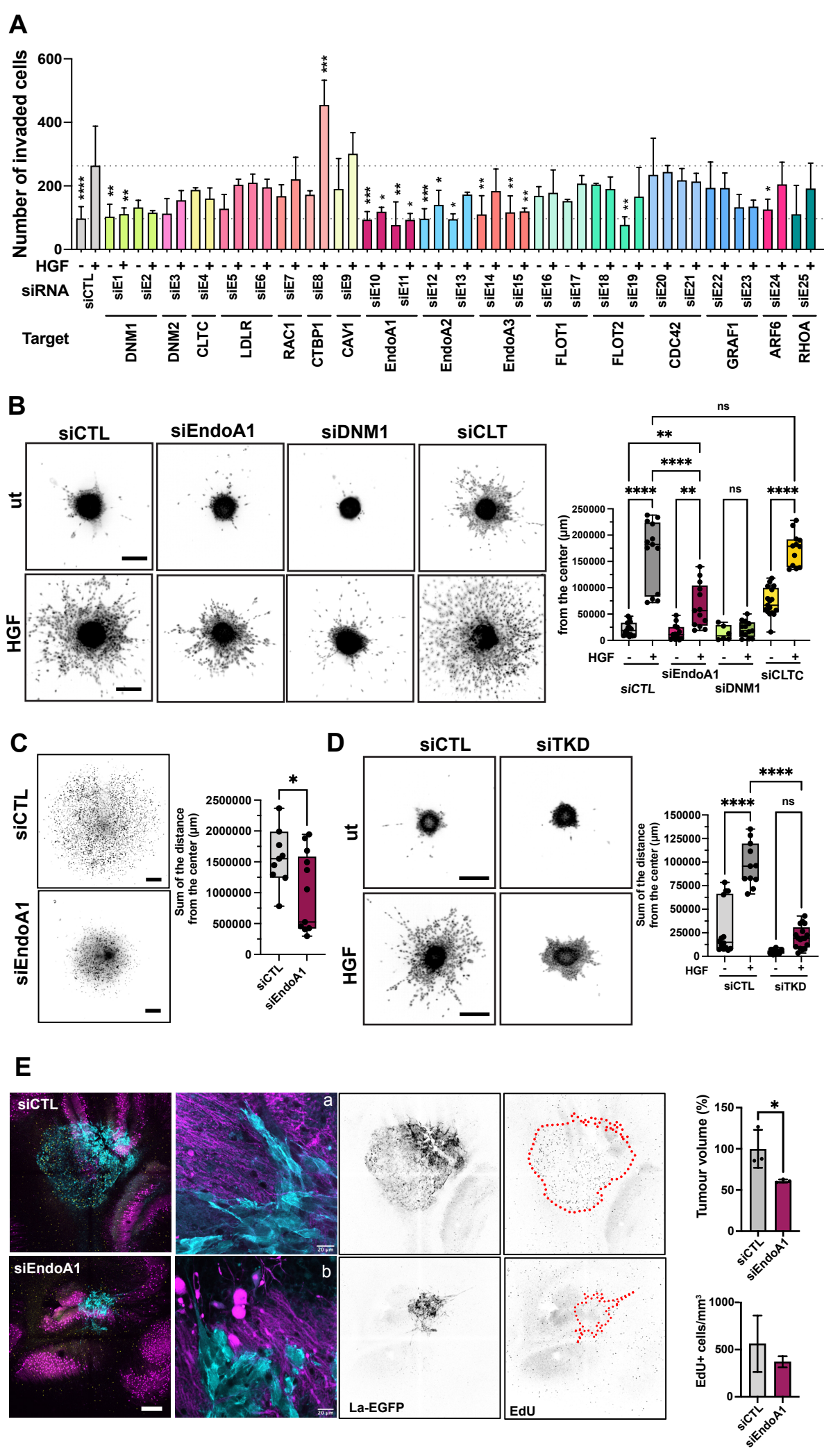
A
Number of invaded cells
600
400
200
0
HGF
siRNA
siCTL
siE1
siE2
siE3
siE4
siE5
siE6
siE7
siE8
siE9
siE10
siE11
siE12
siE13
siE14
siE15
siE16
siE17
siE18
siE19
siE20
siE21
siE22
siE23
siE24
siE25
Target
DNM1
DNM2
CLTC
LDLR
RAC1
CTBP1
CAV1
EndoA1
EndoA2
EndoA3
FLOT1
FLOT2
CDC42
GRAF1
ARF6
RHOA
B
siCTL
siEndoA1
siDNM1
siCLT
ut
HGF
from the center (µm)
ns
siCTL
siEndoA1
siDNM1
siCLTC
C
siCTL
siEndoA1
Sum of the distance from the center (µm)
D
siCTL
siTKD
ut
HGF
E
siCTL
siEndoA1
a
b
La-EGFP
EdU
Tumour volume (%)
EdU+ cells/mm³

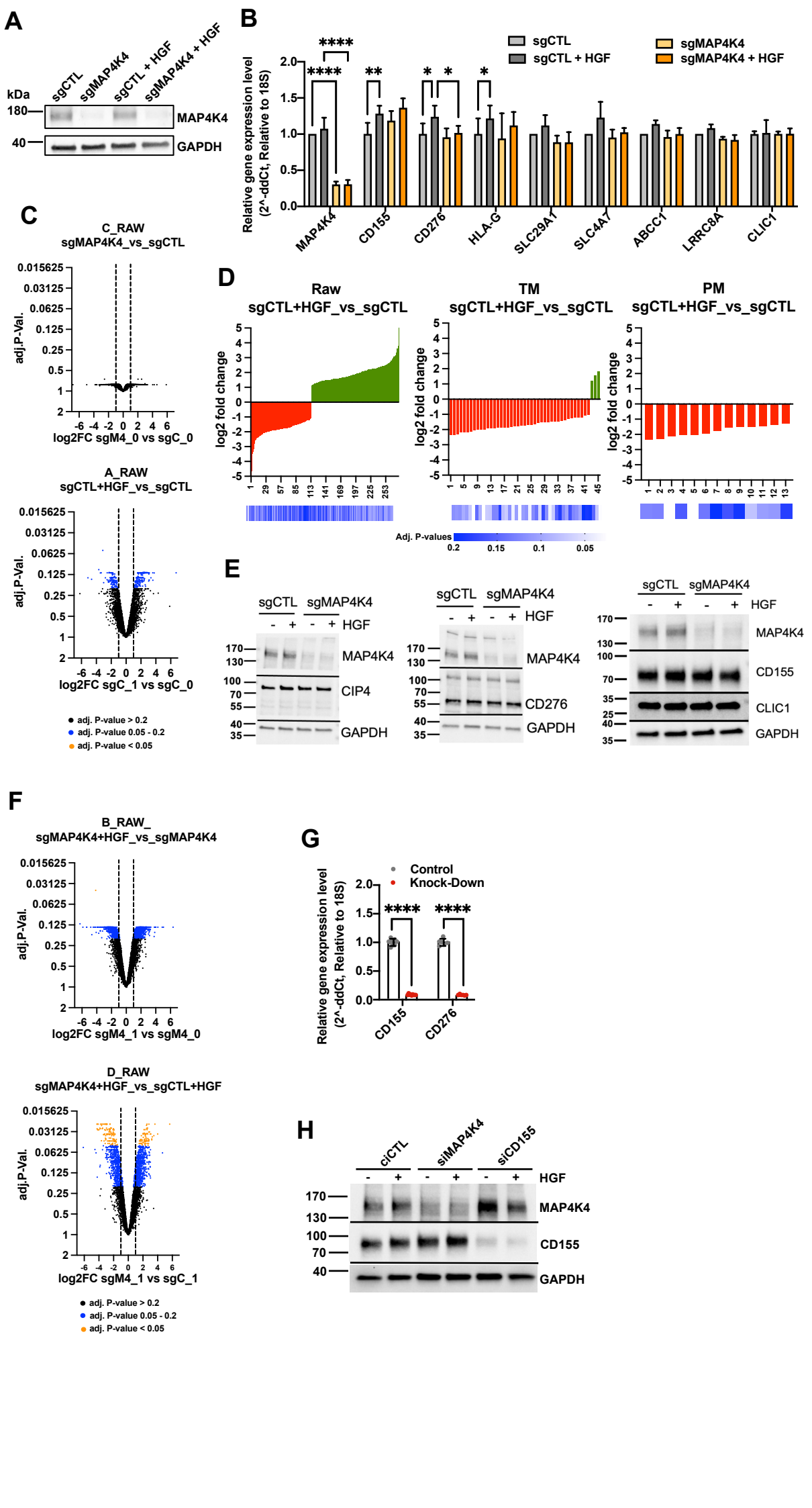
A
sgCTL
sgMAP4K4
sgCTL + HGF
sgMAP4K4 + HGF
kDa
180
40
MAP4K4
GAPDH
B
sgCTL
sgCTL + HGF
sgMAP4K4
sgMAP4K4 + HGF
Relative gene expression level (2^-ddCt, Relative to 18S)
MAP4K4
CD155
CD276
HLA-G
SLC29A1
SLC4A7
ABCC1
LRRC8A
CLIC1
C
C_RAW
sgMAP4K4_vs_sgCTL
adj.P-Val.
log2FC sgM4_0 vs sgC_0
A_RAW
sgCTL+HGF_vs_sgCTL
log2FC sgC_1 vs sgC_0
adj. P-value > 0.2
adj. P-value 0.05 - 0.2
adj. P-value < 0.05
D
Raw
sgCTL+HGF_vs_sgCTL
TM
sgCTL+HGF_vs_sgCTL
PM
sgCTL+HGF_vs_sgCTL
log2 fold change
Adj. P-values
E
sgCTL
sgMAP4K4
HGF
MAP4K4
CIP4
CD276
CD155
CLIC1
GAPDH
F
B_RAW_
sgMAP4K4+HGF_vs_sgMAP4K4
log2FC sgM4_1 vs sgM4_0
D_RAW
sgMAP4K4+HGF_vs_sgCTL+HGF
log2FC sgM4_1 vs sgC_1
G
Control
Knock-Down
Relative gene expression level (2^-ddCt, Relative to 18S)
CD155
CD276
H
ciCTL
siMAP4K4
siCD155
HGF
MAP4K4
CD155
GAPDH

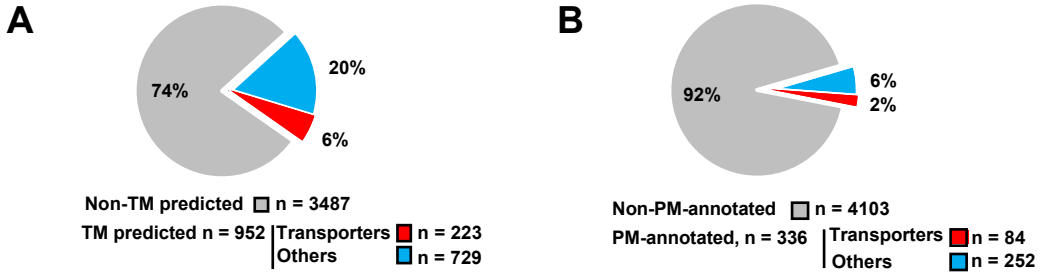


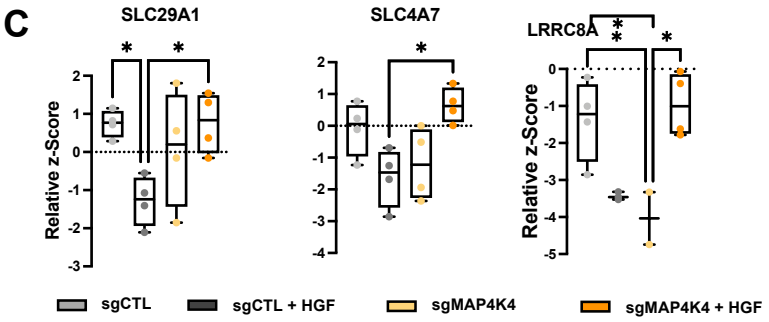


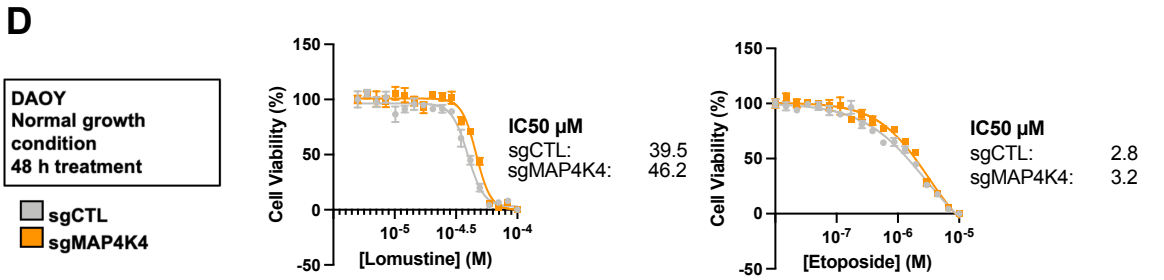


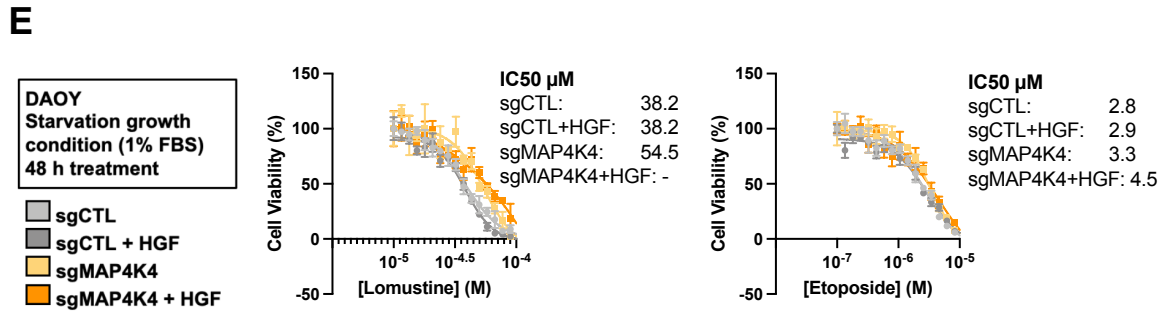


F

| | | | Average Z-score (all-group comparaison) | | | | sgCTL + HGF / sgCTL | | sgMAP4K4 + HGF / sgMAP4K4 | | sgMAP4K4 / sgCTL | | sgMAP4K4 + HGF / sgCTL + HGF | |
|---|---|---|---|---|---|---|---|---|---|---|---|---|---|---|
| Gene | Full Name | Ions | sgCTL | sgCTL + HGF | sgMAP4K4 | sgMAP4K4 + HGF | Log2FC | p-Value | Log2FC | p-Value | Log2FC | p-Value | Log2FC | p-Value |
| CACNA2D1 | calcium voltage-gated channel auxiliary subunit alpha2delta 1 | Ca2+ | 1.76 | 1.94 | 2.49 | 1.14 | 0.19 | 0.74 | -1.35 | 0.07 | 0.76 | 0.23 | -0.80 | 0.24 |
| CLCN3 | chloride voltage-gated channel 3 | H+ \| Cl- | -2.84 | -4.16 | -2.54 | -2.31 | -1.35 | 0.24 | 0.22 | 0.75 | 0.32 | 0.69 | 1.83 | 0.07 |
| CLCN7 | chloride voltage-gated channel 7 | H+ \| Cl- | -1.78 | -2.65 | -3.95 | -2.03 | NA | NA | 1.92 | **0.01** | NA | NA | 0.59 | 0.48 |
| CLIC1 | chloride intracellular channel 1 | Cl- | 1.22 | 1.82 | 2.08 | -0.45 | 0.61 | 0.24 | **-2.52** | **0.00** | 0.89 | 0.16 | **-2.26** | **0.00** |
| CLIC4 | chloride intracellular channel 4 | Cl- | -0.74 | -1.05 | 0.31 | -1.24 | -0.29 | 0.74 | -1.51 | 0.10 | 1.09 | 0.27 | -0.15 | 0.83 |
| CLIC6 | chloride intracellular channel 6 | Cl- | -2.01 | -3.59 | -2.79 | -2.05 | -1.54 | 0.08 | 0.77 | 0.53 | -0.77 | 0.42 | NA | NA |
| CLCC1 | chloride channel CLIC like 1 | Cl- | 3.87 | 3.55 | 3.61 | 3.63 | -0.30 | 0.40 | 0.02 | 0.96 | -0.24 | 0.54 | 0.06 | 0.88 |
| CLNS1A | chloride nucleotide-sensitive channel 1A | Cl- | -1.75 | 0.22 | -1.14 | -3.71 | 1.97 | 0.07 | **-2.49** | **0.03** | 0.63 | 0.63 | **-3.87** | **0.00** |
| CNGB1 | cyclic nucleotide gated channel subunit beta 1 | Cation | -1.06 | 0.25 | -0.73 | -1.74 | 1.32 | 0.23 | -0.98 | 0.09 | 0.36 | 0.58 | -1.97 | 0.07 |
| CRACR2A | calcium release activated channel regulator 2A | Ca2+ | -2.45 | -3.03 | -2.73 | -3.00 | -0.57 | 0.43 | -0.14 | 0.87 | -0.27 | 0.72 | 0.13 | 0.87 |
| KCNMA1 | potassium calcium-activated channel subfamily M alpha 1 | Ca2+ \| K+ | -0.98 | -2.35 | -1.81 | 0.63 | -1.35 | 0.18 | 2.48 | 0.05 | -0.81 | 0.56 | 2.99 | **0.00** |
| PACC1 | proton activated chloride channel 1 | Cl- | -3.10 | -3.14 | -2.64 | -3.51 | 0.03 | 0.97 | -0.80 | 0.29 | 0.49 | 0.36 | -0.32 | 0.71 |
| TMC5 | transmembrane channel like 5 | Ca2+ \| Cl- | 3.58 | 4.40 | 4.75 | 3.51 | 0.84 | 0.08 | -1.26 | 0.06 | 1.20 | 0.08 | **-0.92** | **0.04** |
| VDAC1 | voltage dependent anion channel 1 | Anion | 1.43 | 0.92 | 1.38 | 1.91 | -0.49 | 0.38 | 0.54 | 0.47 | -0.03 | 0.96 | 0.98 | 0.19 |
| VDAC2 | voltage dependent anion channel 2 | Anion | 3.30 | 3.13 | 3.32 | 3.82 | -0.15 | 0.80 | 0.50 | 0.35 | 0.04 | 0.94 | 0.66 | 0.17 |
| VDAC3 | voltage dependent anion channel 3 | Anion | -0.09 | -1.07 | 0.52 | 0.96 | -0.96 | 0.21 | 0.46 | 0.61 | 0.64 | 0.44 | 2.04 | **0.03** |
| ATP1A1 | ATPase Na+/K+ transporting subunit alpha 1 | Na+ \| K+ | 7.42 | 6.57 | 6.82 | 8.07 | -0.84 | 0.12 | 1.23 | 0.06 | -0.58 | 0.36 | 1.44 | **0.01** |
| ATP1B1 | ATPase Na+/K+ transporting subunit beta 1 | Na+ \| K+ | 4.42 | 3.89 | 4.33 | 3.95 | -0.51 | 0.24 | -0.40 | 0.45 | -0.06 | 0.89 | 0.03 | 0.96 |
| ATP1A3 | ATPase Na+/K+ transporting subunit alpha 3 | Na+ \| K+ | -1.42 | -2.52 | -2.08 | 0.10 | -1.09 | 0.13 | 2.22 | 0.05 | -0.66 | 0.58 | 2.64 | **0.00** |
| ATP12A | ATPase H+/K+ transporting non-gastric alpha2 subunit | K+ \| K+ | 2.54 | 1.56 | 2.34 | 3.36 | -0.98 | 0.07 | 1.01 | 0.12 | -0.21 | 0.73 | 1.79 | **0.00** |
| ATP1B3 | ATPase Na+/K+ transporting subunit beta 3 | Na+ \| K+ | 5.63 | 5.83 | 6.19 | 4.95 | 0.20 | 0.59 | -1.27 | 0.05 | 0.58 | 0.20 | -0.92 | 0.11 |
| ATP2B1 | ATPase plasma membrane Ca2+ transporting 1 | Ca2+ | 1.78 | 0.67 | 0.59 | 3.68 | -1.09 | 0.13 | 3.11 | 0.02 | -1.17 | 0.14 | 3.00 | **0.02** |
| ATP6AP2 | ATPase H+ transporting accessory protein 2 | H+ | -0.16 | -0.67 | 0.72 | -0.29 | -0.50 | 0.29 | -0.99 | 0.10 | 0.90 | **0.05** | 0.39 | 0.51 |

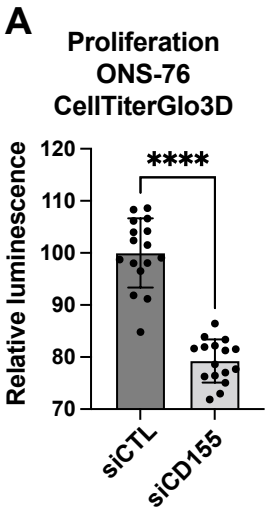
A
Proliferation
ONS-76
CellTiterGlo3D
Relative luminescence
120
110
100
90
80
70
****
siCTL
siCD155

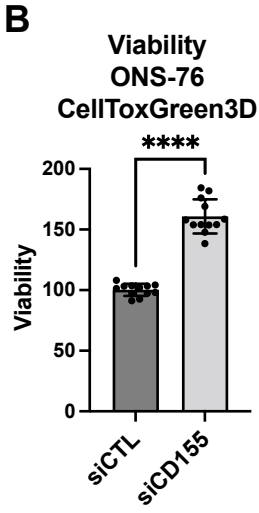
B
Viability
ONS-76
CellToxGreen3D
Viability
200
150
100
50
0
****
siCTL
siCD155

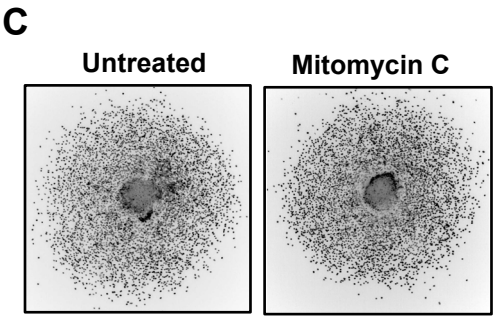
C
Untreated
Mitomycin C

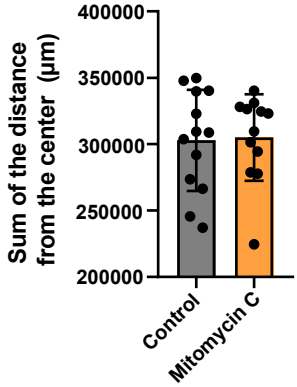
Sum of the distance
from the center (µm)
400000
350000
300000
250000
200000
Control
Mitomycin C

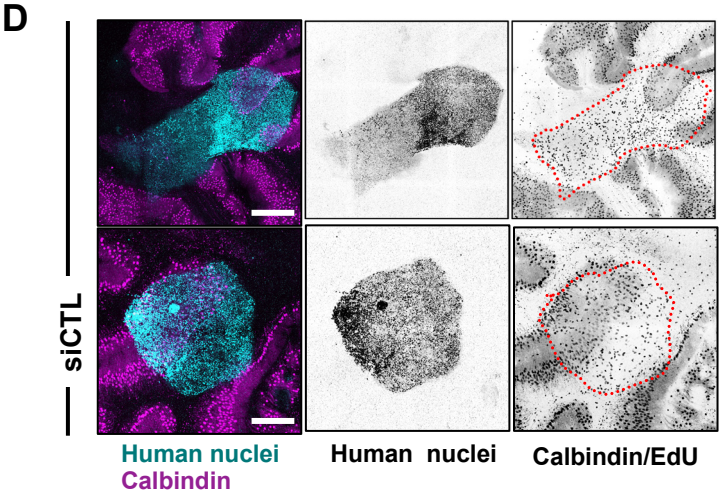
D
siCTL
Human nuclei
Calbindin
Human nuclei
Calbindin/EdU

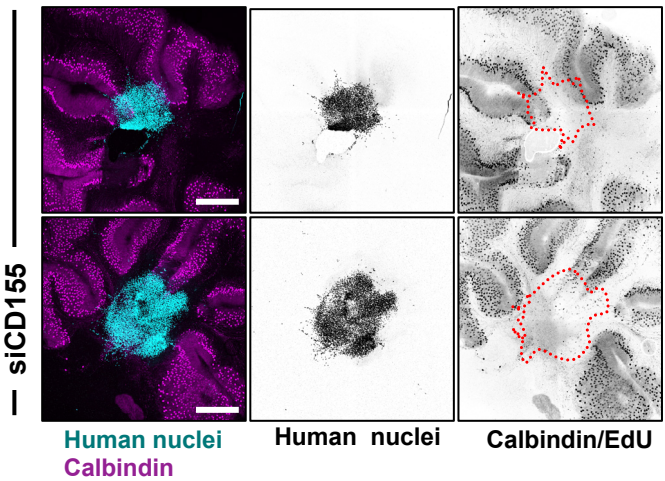
siCD155
Human nuclei
Calbindin
Human nuclei
Calbindin/EdU

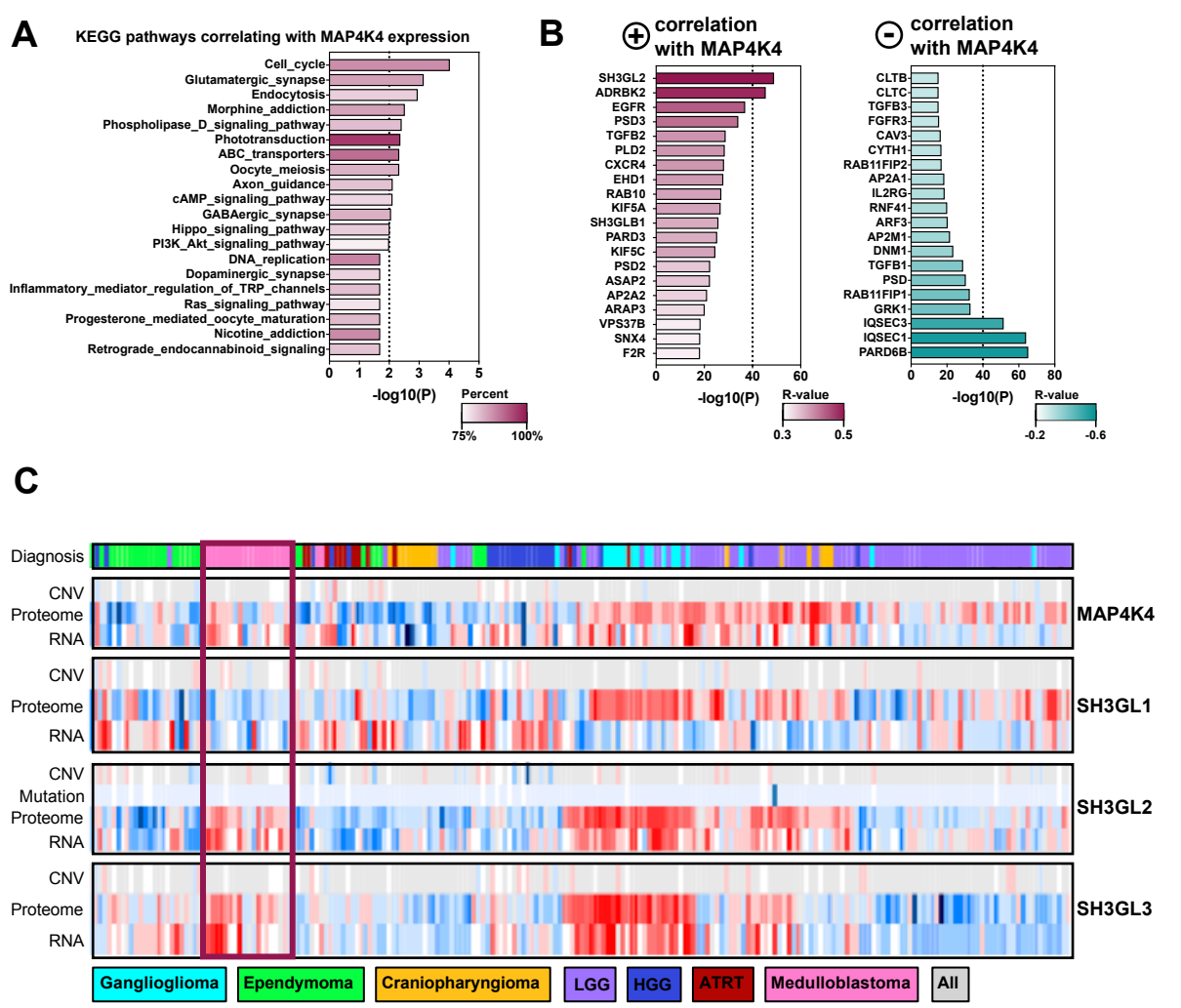
A
KEGG pathways correlating with MAP4K4 expression
Cell_cycle
Glutamatergic_synapse
Endocytosis
Morphine_addiction
Phospholipase_D_signaling_pathway
Phototransduction
ABC_transporters
Oocyte_meiosis
Axon_guidance
cAMP_signaling_pathway
GABAergic_synapse
Hippo_signaling_pathway
PI3K_Akt_signaling_pathway
DNA_replication
Dopaminergic_synapse
Inflammatory_mediator_regulation_of_TRP_channels
Ras_signaling_pathway
Progesterone_mediated_oocyte_maturation
Nicotine_addiction
Retrograde_endocannabinoid_signaling
0 1 2 3 4 5
-log10(P)
Percent
75% 100%
B
correlation with MAP4K4
SH3GL2
ADRBK2
EGFR
PSD3
TGFB2
PLD2
CXCR4
EHD1
RAB10
KIF5A
SH3GLB1
PARD3
KIF5C
PSD2
ASAP2
AP2A2
ARAP3
VPS37B
SNX4
F2R
0 20 40 60
-log10(P)
R-value
0.3 0.5
correlation with MAP4K4
CLTB
CLTC
TGFB3
FGFR3
CAV3
CYTH1
RAB11FIP2
AP2A1
IL2RG
RNF41
ARF3
AP2M1
DNM1
TGFB1
PSD
RAB11FIP1
GRK1
IQSEC3
IQSEC1
PARD6B
0 20 40 60 80
-log10(P)
R-value
-0.2 -0.6
C
Diagnosis
CNV
Proteome
RNA
MAP4K4
CNV
Proteome
RNA
SH3GL1
CNV
Mutation
Proteome
RNA
SH3GL2
CNV
Proteome
RNA
SH3GL3
Ganglioglioma
Ependymoma
Craniopharyngioma
LGG
HGG
ATRT
Medulloblastoma
All

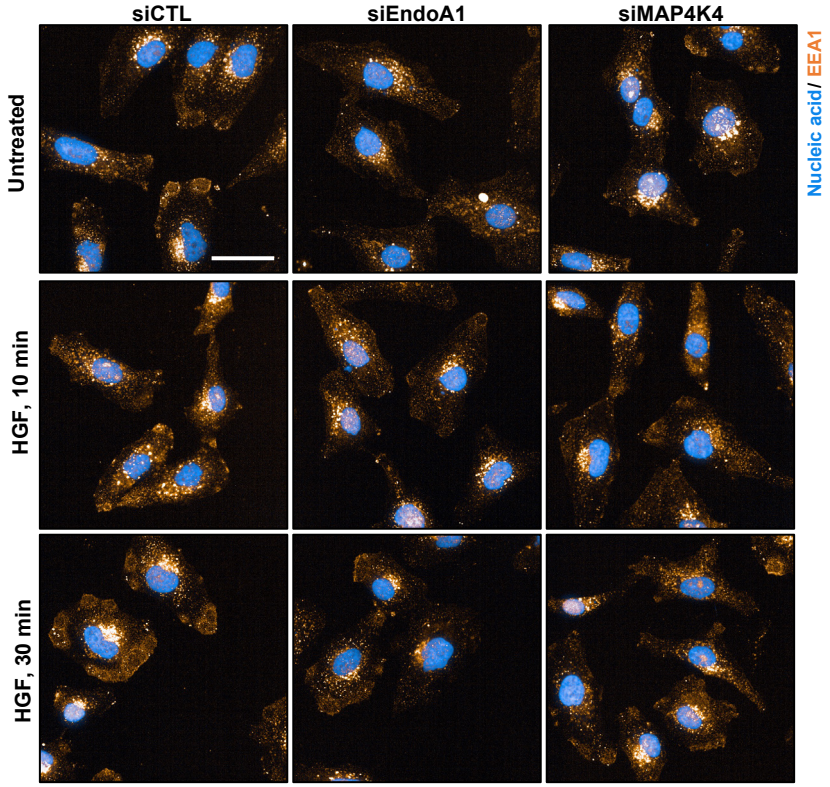
siCTL
siEndoA1
siMAP4K4
Untreated
HGF, 10 min
HGF, 30 min
Nucleic acid / EEA1

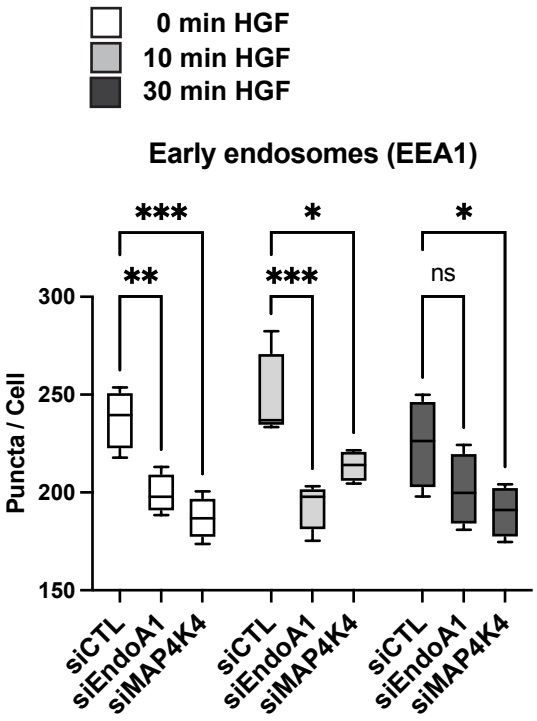
0 min HGF
10 min HGF
30 min HGF
Early endosomes (EEA1)
Puncta / Cell
300
250
200
150
***
**
*
***
*
ns
siCTL
siEndoA1
siMAP4K4
siCTL
siEndoA1
siMAP4K4
siCTL
siEndoA1
siMAP4K4

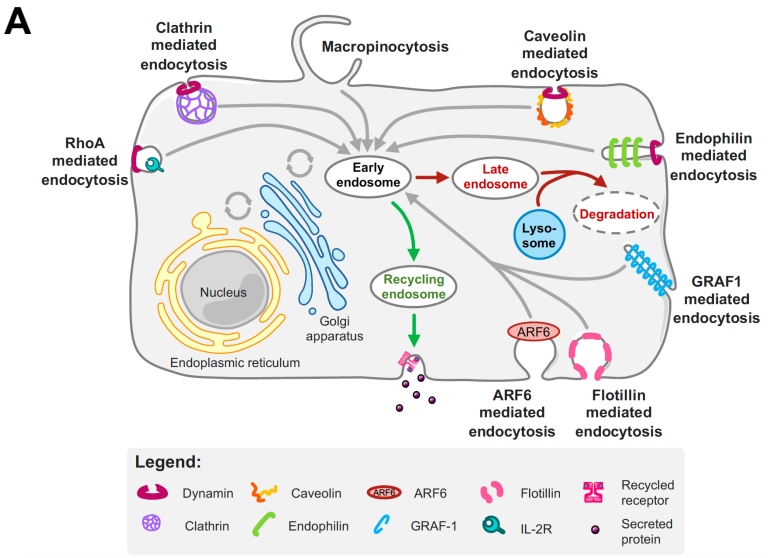


B

| siRNA | Gene | Endocytic pathway |
|---|---|---|
| siE1 | DNM1 | Broad spectrum endocytosis |
| siE2 | | |
| siE3 | DNM2 | |
| siE4 | CLTC | Clathrin mediated endocytosis |
| siE5 | LDLR | |
| siE6 | | |
| siE7 | RAC1 | Macropinocytosis* |
| siE8 | CTBP1 | |
| siE9 | CAV1 | Caveolin mediated endocytosis |
| siE10 | SH3GL2 | Endophilin mediated endocytosis |
| siE11 | | |
| siE12 | SH3GL1 | |
| siE13 | | |
| siE14 | SH3GL3 | |
| siE15 | | |
| siE16 | FLOT1 | Flotillin mediated endocytosis* |
| siE17 | | |
| siE18 | FLOT2 | |
| siE19 | | |
| siE20 | CDC42 | GEEC-CCLIC endocytosis* |
| siE21 | | |
| siE22 | GRAF1 | |
| siE23 | | |
| siE24 | ARF6 | Arf6 mediated endocytosis* |
| siE25 | RHOA | Rho/IL-2R endocytosis |
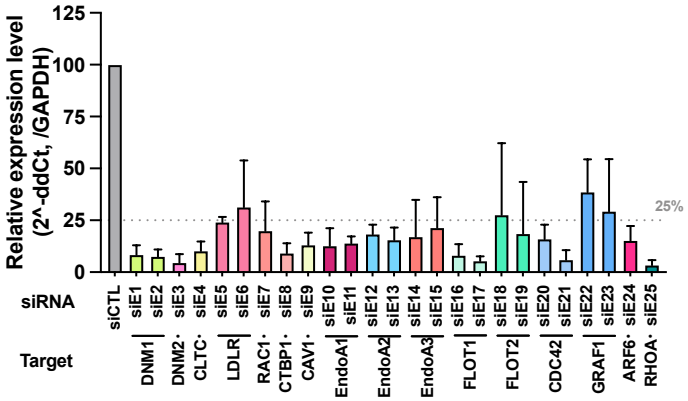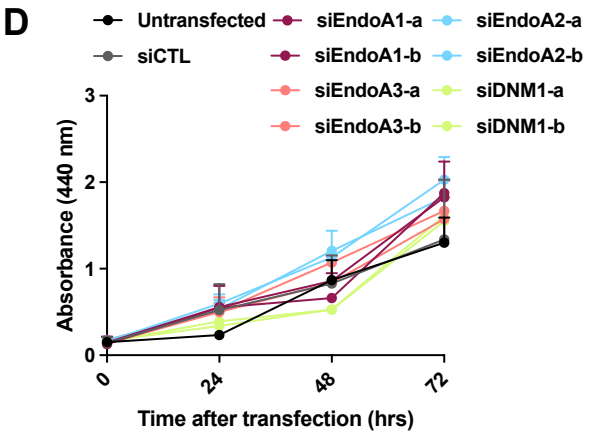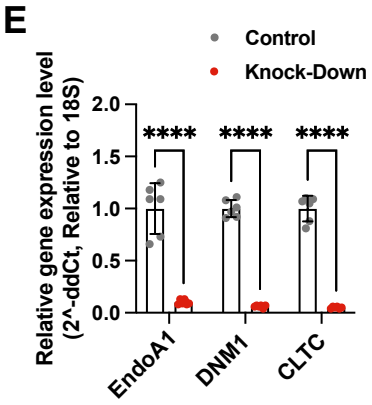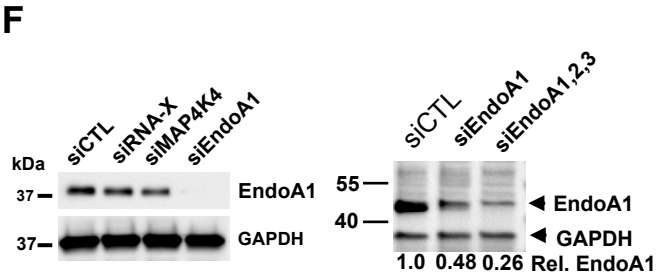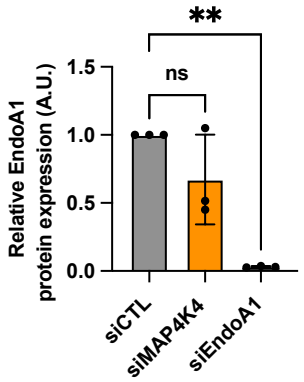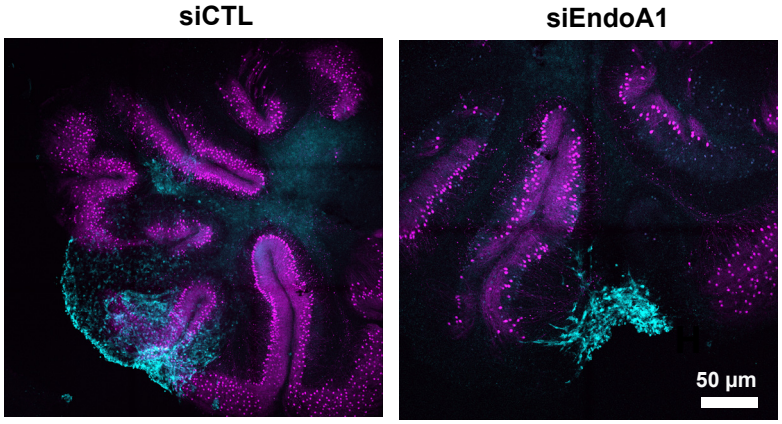
*Dynaminin-independent endocytic pathway